CHALMERS

New Algorithms for Dynamical Mean Field Theory

Master of Science Thesis in Fundamental Physics

SAM VAJEDI

Chalmers University of Technology
University of Gothenburg
Department of Fundamental Physics
Göteborg, Sweden, 2013

New Algorithms for Dynamical Mean Field Theory

Sam Vajedi

Examiner: Stellan Östlund

Chalmers University of Technology
University of Gothenburg
Department of Fundamental Physics
SE-412 96 Göteborg
Sweden

Department of Fundamental Physics
Göteborg, Sweden, 2013

Acknowledgements

Materials with strongly correlated fermions and the physics of these systems has been a great challenge to understand fully. There are many phenomena that cannot yet be explained accurately enough, such as high-temperature superconductivity. Strongly correlated systems are mathematically very hard to model since one cannot simply neglect the interactions between the particles in order to predict their behavior. This made me intrigued to learn more about these systems and study the theoretical and numerical tools that have been used so far in describing them.

I would like to thank my supervisors Stellan Östlund and Mats Granath for inspiring me and for giving me the opportunity to work in the field of strongly correlated fermions. Hugo Strand, Andro Sabashvili and Matteo Bazzanella have also played an important role in my studies when trying to understand many-body theory. I want to thank Johan Schött for providing the figure illustrating the MaxEnt solution of the density of states.

My gratitude also extends to my family and friends, who always stand by me and give support.

New Algorithms for Dynamical Mean Field Theory

SAM VAJEDI
Department of Fundamental Physics
Chalmers University of Technology

Abstract

In this thesis single particle Green's functions in quantum many particle physics are studied. The Green's function gives us the density of states which is an important characteristic distinguishing for example a metal from an insulator. For systems with strongly correlated electrons the Green's function cannot in general be computed exactly. One approximation scheme, called the dynamical mean-field theory (DMFT), has been used to investigate such systems.

In its most common form, DMFT analyzes the problem on frequencies on the imaginary axis, while the physical properties are functions of frequencies on the real axis. The first problem is therefore to investigate an analytical continuation to transform Green's functions of purely imaginary frequencies to Green's functions of real frequencies. The stability of the Padé approximants, used for such a transformation, is examined by applying some noise to the input functions.

It is found that the error of the Padé approximation increases linearly with respect to the noise, up to a crucial point where for larger noise the error of the output does not change. It is verified that a first and second order Taylor expansion of the analytic continuation cannot explain this phenomenon; they can only explain the linear behavior at small noise levels.

In the second part of the thesis a different method, called the distributional exact diagonalization method is used which directly computes the self-energy in the complex frequency plane; no analytic continuation is therefore needed. The method is used to calculate the spectral function for a Mott insulator at zero temperature with the chemical potential $\mu = U/2$, where U is the interaction energy.

The spectral function of the Mott insulator contains two Hubbard bands located at $\pm U/2$, which is in agreement with previous results. When the interaction energy $U = 4$, two peaks are shown in addition to the Hubbard bands, but no peaks are shown for $U = 10$. This kind of behavior can be seen when using the distributional exact diagonalizition method, while if one uses some impurity solver that requires analytic continuation, this information might be lost in the process. The results seem to imply that distributional exact diagonalizing is a good method for capturing real-frequency structure within DMFT.

Keyword: Many-body Systems, Strongly Correlated Fermions, DMFT, Analytic Continuation, DistED, Padé Approximation.

Contents

1 Introduction

Many approximation schemes and numerical methods have been developed to overcome the difficulties related to strongly correlated systems. One of them is dynamical mean field theory (DMFT) [1]. It is applicable to strongly correlated electrons in solids and cold atoms in optical lattices [2], and it has seen much success in explaining for instance the behavior of Mott insulators, Mott transition and phase separation.

DMFT has some similarities with the classical mean field theory (MFT); they both map a many-body lattice problem onto a local single-site problem. MFT can be used for the Ising model to reduce the magnetic field to an effective mean field, thus reducing a many-body problem to a one-body problem. DMFT, on the other hand, maps a quantum many-body lattice problem, like the Hubbard model, to a local (Anderson) impurity model, with a self-consistency condition. The impurity models are in general more easily solvable by various methods: quantum Monte Carlo, exact diagonalization, iterative perturbation scheme, and so on.

The DMFT equations are in their most common form written in terms of Green's functions defined in the imaginary Matsubara frequency space, which are just the Fourier transforms of the imaginary time Green's functions. A finite temperature Green's function is the key object in many-body physics and characterizes a wide range of experimentally accessible observables.

Solving the DMFT equations yields, in many cases, Green's functions and self-energy as function of imaginary frequencies, but physical observables are calculated using the real time Green's functions. Thus, analytic continuation has to be performed in order to transform the imaginary time Green's functions from the imaginary time axis to the real time axis. Since we only know the values of the Green's functions at a finite set of the Matsubara frequencies it is not trivial to do the analytic continuation numerically. A widely used technique to handle this problem is by applying the Padé approximant method.

Since this procedure is very unstable, one would contrary to this expectation expect the Padé method to be extremely dependent on the accuracy of the input data. This would imply that if the input data is not accurate enough it can lead to non-physical results. (The acquired precision depends on the temperature and number of poles used in the method.)

When applying some noise the analytic continuation behaves surprisingly stable; input data with high noise still gives reasonable results. The aim of the first part of the thesis is therefore to investigate the analytic continuation

by Padé approximation of the Matsubara data to explain why the method is stable even though the singular values of the Jacobian turns out to indicate the opposite.

The second part of the thesis presents the results of calculating the full analytic self-energy in the complex frequency plane. The method that is used for this is a distributional exact diagonalization method (DistED method) for quantum impurity models, which was developed by M. Granath and H. U. R. Strand [3]. This method is especially useful for computing real frequencies of self-energy, and therefore there is no need of analytic continuation from imaginary frequencies. In this thesis the distributional exact diagonalization formalism is applied to systems with strongly correlated electrons in a Mott insulator, within DMFT.

1.1 Outline

This thesis starts by introducing the basic concept of Green's functions and the spectral functions in Chapter 2. Some crucial relations are derived, and the non-interaction Green's function and the spectral function of the non-interaction Hamiltonian are calculated. In Chapter 3 the analytic continuation, using the Padé approximant, is described. Later in this chapter a spectral function is derived from the one-dimensional, tight-binding Hamiltonian and used as a test function to investigate the accuracy of the analytic continuation.

In Chapter 4 the stability of the transformation from Green's functions of imaginary time to Green's functions of real time is covered. This is done by studying the first order approximation and the singular values of the Jacobian, and then investigating the second order approximation. Chapter 5 summarizes part I of this thesis.

In Chapter 6 the dynamical mean field theory is presented. Exact diagonalization (as well as Anderson model mapping) is introduced as a way to calculate the local interacting Green's function G_I. In Chapter 7 DistED algorithms are covered using what is already known from exact diagonalization. Later in that chapter, some important aspects of the Mott metal-insulator transition are explained, and the self-energy for real values is calculated by applying distributional exact diagonalization. A discussion about the results and some comparisons with earlier results are made in the end of this chapter.

1.2 Background

It has been known for some time how to explain the properties of materials with weakly correlated electrons, such as simple metals, some semiconductors and insulators. Using band theory one is able to predict is in these

cases whether or not a material is conducting, semiconducting or insulating. Materials with open shells, i.e. materials for which not all states in the shell are occupied, are conducting, while materials with filled shells and with an energy gap to the next unoccupied state are insulating. Several techniques exist to calculate various microscopic properties of materials with weakly correlated electrons. The density functional theory (DFT) is the main technique for such systems. It allows us to calculate the total energy by mapping a many-body problem of interacting quantum mechanical particles to a non-interacting Kohn-Sham reference system with a density dependent single-particle effective potential [4].

DFT gives high accuracy for the ground state of wide-band metallic and insulating systems when the temperature is zero, but has problems with systems closer to the atomic limit containing partially filled narrow bands, and where the electron-electron interaction has a more dominant role.

Band theory also fails to explain the behavior of materials with open shells where the electrons occupy narrow orbitals. In these materials the strong Coulombic repulsion, caused by the spatial confinement of electrons that occupy narrow orbitals, makes it impossible to treat the electrons independently.

Neville Mott discussed in his paper 1937 [5] that insulators can be understood by thinking of them as a collection of localized electrons bound to atoms with partially filled shells. To describe strongly correlated systems one has to consider this localization of electrons, but they can also be treated as delocalized plane waves. Models for strongly correlated systems must therefore include the components of the real-space and momentum-space picture. This makes strongly correlated systems difficult to model. One of the simplest ways to treat these systems is to take into account only the electron orbitals near the Fermi level and only incorporate in an effective Hamiltonian.

The Hubbard model [6] is often used to capture localized and delocalized behaviors of the electrons, and is defined by

$$H_{\text{Hub}} = \sum_{ij,\sigma} t_{ij} c^{\dagger}_{i\sigma} c_{j\sigma} + U \sum_{i} n_{i\uparrow} n_{j\downarrow}. \tag{1.1}$$

H_{Hub} describes electrons moving between localized states at lattice sites i and j with spin $\uparrow$ or $\downarrow$. The hopping term $t_{i,j}$ contains the delocalized behavior of the electrons while the local Coulomb repulsion energy U gives the localized behavior, and these terms compete. If $t_{i,j}$ is much larger than U then the electrons will move freely between the atoms, as in metals. For large U two electrons are prevented from occupying the same site and may therefore be more localized on the site (in materials with half-filled shells the electrons will be fully localized).

The Hubbard model and the DMFT solution for strongly correlated electrons are discussed in more detail in Chapter 6. Here a mathematical de-

scription is needed of the lifetime of the electron occupancy at a particular site, which is done using Green's function of imaginary time. This will be further discussed in the next chapter.

2 Matsubara Green's Functions and Spectral Functions

Green's functions appear as natural quantities to characterize many-particle systems. They are closely related to experimental observables and have therefore many applications. However, in most cases it is very complicated to calculate Green's functions exactly, and instead one has to use perturbation theory or other approximation methods [7].

Green's functions are extensively used in this thesis, and this chapter therefore introduces the Green's functions that are necessary when working with strongly correlated fermions. Important properties are also derived and some concept are given of how to treat the Green's functions.

Various definitions of Green's functions will now be presented, and we first consider the general case of an n-body real-time Green's function in the Grand Canonical Ensemble and in the Heisenberg representation:[1]

$$\begin{aligned} &G^{(n)}(x_1t_1,\cdots x_nt_n;x_1't_1',\cdots x_n't_n') = \\ &= (-i)^n\langle T\psi(x_1t_1)\cdots\psi(x_nt_n)\psi^\dagger(x_nt_n)\cdots\psi^\dagger(x_1t_1)\rangle, \end{aligned}$$

where $\psi(x,t) \equiv e^{i(H-\mu N)t}\psi(x)e^{-i(H-\mu N)t}$ and $\langle\cdot\rangle$ is the thermal average.

The retarded and advanced Green's functions are given by the two point functions [8]

$$\begin{aligned} G^R(rt,r't') &\equiv -i\theta(t-t')\langle\{\psi(rt),\psi(r't')\}\rangle, \\ G^A(rt,r't') &\equiv i\theta(t'-t)\langle\{\psi(rt),\psi(r't')\}\rangle. \end{aligned}$$

The propagation of one particle at the ground state $|\psi_0\rangle$ is described by a two-point Green's function and is defined by

$$G(rt;r't') = -\frac{i}{\hbar}\langle\psi_0|T\psi(r,t)\psi^\dagger(r',t')|\psi_0\rangle, \tag{2.1}$$

where T is the time ordering operator which is given by the following relation:

$$T\psi(r,t)\psi^\dagger(r',t') = \begin{cases} \psi(r,t)\psi^\dagger(r',t') & \text{for} \quad t > t' \\ \pm\psi^\dagger(r',t')\psi(r,t) & \text{for} \quad t' > t. \end{cases}$$

[1] If the imaginary-time Heisenberg representation is used we let $t \to \tau$ and skip the factor of $(-i)^n$.

We have here chosen to only consider fermions.

It is difficult to evaluate the time evolution operators, $e^{it(H-\mu N)}$, perturbatively because the calculation to invert from Fourier transform involves integral in complex plane. To make the calculation easier one can define a Green's function, called Matsubara Green's function, that is a time-ordered product along the imaginary axis. The Matsubara Green's function will later be connected with the retarded Green's function, which is used to calculate physical observables.

The Matsubara Green's function is defined by

$$\mathcal{G}(r,r';\tau-\tau') = -\langle T_\tau \psi(r,\tau)\psi(r',\tau')\rangle,$$

where $-\beta < \tau - \tau' < \beta$. The time evolution operators are defined by

$$\psi(r,\tau) \equiv e^{\tau K}\psi(r)e^{-\tau K},$$
$$\psi^\dagger(r,\tau) \equiv e^{\tau K}\psi^\dagger(r)e^{-\tau K},$$

where $K = H - \mu N$. The time evolution operators are here the same as before, but we now use the imaginary time $\tau = it$.

The Matsubara Green's function has an antiperiodic property which can be proved by calculating

$$\begin{aligned}\mathcal{G}(r,r';\tau+\beta) &= \frac{-1}{Z}\mathrm{Tr}[e^{-\beta H}e^{(\tau+\beta)H}\psi(r)e^{-(\tau+\beta)H}\psi(r')] = \\ &= \frac{-1}{Z}\mathrm{Tr}[e^{\tau H}\psi(r)e^{-\tau H}e^{-\beta H}\psi(r')] = \\ &= \frac{-1}{Z}\mathrm{Tr}[e^{-\beta H}\psi(r')e^{\tau H}\psi(r)e^{-\tau H}] = \\ &= \frac{-1}{Z}\mathrm{Tr}[e^{-\beta H}T_\tau\psi(r,\tau)\psi(r')] = -\mathcal{G}(r,r';\tau),\end{aligned}$$

when $\tau < 0$. In the same way, one can prove that

$$\mathcal{G}(r,r';\tau-\beta) = -\mathcal{G}(r,r';\tau)$$

when $\tau > 0$. This property is used to expand the Green's function in a Fourier series that will automatically satisfy the property. The Green's function becomes

$$\mathcal{G}(r,r';\tau) = \frac{1}{\beta}\sum_{n=-\infty}^{\infty} e^{-i\omega_n\tau}\mathcal{G}(r,r';i\omega_n), \tag{2.2}$$

where we now have introduced the Matsubara frequencies for fermions, $\omega_n = (2n+1)\pi/\beta$.

From (2.2) one finds

$$\mathcal{G}(r,r';i\omega_n) = \int_0^\beta \mathrm{d}\tau e^{i\omega_n\tau}\mathcal{G}(r,r';\tau). \tag{2.3}$$

To derive the relation between $G^R(r,t;r',t')$ and $\mathcal{G}(r,r';i\omega_n)$ we will first introduce the spectral representation for G^R and $\mathcal{G}$. The spectral function is defined by

$$A(r,r';t) \equiv \left\langle \{\psi(r,t), \psi^\dagger(r',0)\} \right\rangle, \tag{2.4}$$

and we can therefore express the retarded Green's function as $G^R(r,r';t) = -iA(r,r';t)\theta(t)$. The spectral representation is obtained by taking the Fourier transform of our rewritten G^R:

$$G^R(r,r';\omega) = \int_{-\infty}^{\infty} \frac{\mathrm{d}\omega'}{2\pi} \frac{A(r,r';\omega')}{\omega + i\eta - \omega'}.$$

Now, when the spectral representation of G^R is determined, the next step is to calculate the spetral repesentation of $\mathcal{G}$. From (2.3) we get

$$\begin{aligned}
\mathcal{G}(r,r';i\omega_n) &= \int_0^\beta \mathrm{d}\tau e^{-i\omega_n\tau} \left[-\langle \psi(r,\tau)\psi^\dagger(r',0)\rangle \right] = \\
&= \int_0^\infty \mathrm{d}(it) e^{-i\omega_n(it)} \left[-\langle e^{iKt}\psi(r)e^{-iKt}\psi^\dagger(r',0)\rangle \right] + \\
&+ \int_\infty^0 \mathrm{d}(it) e^{-i\omega_n i(t-i\beta)} \left[-\langle e^{iK(t-i\beta)}\psi(r)e^{-iK(t-i\beta)}\psi^\dagger(r',0)\rangle \right] = \\
&= \ldots = -i\int_0^\infty \mathrm{d}t \left\langle \{\psi(r,t), \psi^\dagger(r',0)\} \right\rangle e^{i(i\omega_n)t}.
\end{aligned}$$

Using the definition of the spectral function in (2.4) gives

$$\mathcal{G}(r,r';i\omega_n) = \int_{-\infty}^{\infty} \frac{\mathrm{d}\omega'}{2\pi} \frac{A(r,r';\omega')}{i\omega_n - \omega'}. \tag{2.5}$$

We have now obtained the spectral representations of both G^R and $\mathcal{G}$. Comparing these results gives us the relation

$$G^R(r,r';\omega) = \lim_{i\omega_n \to \omega + i\eta} (\mathcal{G}(r,r';i\omega_n)). \tag{2.6}$$

The mapping of a Green's function of imaginary frequencies, $i\omega_n$, to real frequencies, ω, is what we refer to as an analytic continuation. Note that $\mathcal{G}(r,r';i\omega_n)$ was calculated under the assumption that $\omega_n > 0$. If one instead assumes that $\omega_n < 0$ another relation is obtained:

$$G^A(r,r';\omega) = \lim_{i\omega_n \to \omega - i\eta} (\mathcal{G}(r,r';i\omega_n)). \tag{2.7}$$

Combining the definition of the spectral function with (2.6) and (2.7) yields

$$\begin{aligned}
A(r,r';\omega) &= i\lim_{\eta\to 0}[G(r,r';\omega+i\eta) - G(r,r';\omega-i\eta)] \\
\Rightarrow A(r,r';\omega) &= -2\mathrm{Im}[G^R(r,r';\omega)]
\end{aligned}$$

For translationally invariant systems it is better to define the Matsubara Green's function in momentum space. Rewriting $\mathcal{G}(r,r';\tau-\tau')$ using momentum and real space second quantized operators one obtains

$$\mathcal{G}(k,\tau-\tau') = -\langle T_\tau c_k(\tau) c_k^\dagger(\tau')\rangle.$$

This definition is used to calculate the Matsubara Green's function in momentum space of a non-interacting system, which is governed by the Hamiltonian

$$H_0 = \sum_k (\varepsilon_k - \mu) c_k^\dagger c_k.$$

Firstly, we need to calculate $c_k(\tau)$ by solving the Heisenberg equation of motion,

$$\begin{aligned}&\frac{\partial c_k}{\partial \tau} = [H_0,c_k] = \{H_0,1\}c_k - 1\{H_0,c_k\} = -(\varepsilon_k-\mu)c_k\\ &\Rightarrow c_k(\tau) = e^{-(\varepsilon_k-\mu)\tau}c_k.\end{aligned}$$

The Green's function in momentum space becomes

$$\mathcal{G}(k,\tau) = -\langle T_\tau c_k(\tau) c^{\dagger_k}\rangle = -e^{-(\varepsilon_k-\mu)\tau}[\langle c_k c_k^\dagger\rangle\theta(\tau) - [\langle c_k^\dagger c_k\rangle\theta(-\tau)].$$

We now apply some standard results from elementary statistical mechanics, such as

$$\langle c_k^\dagger c_k\rangle = \frac{1}{e^{\beta(\varepsilon_k-\mu)}+1} \quad \text{and} \quad \langle c_k c_k^\dagger\rangle = 1 - \langle c_k^\dagger c_k\rangle,$$

to the non-interacting Green's function in momentum space:

$$\begin{aligned}\mathcal{G}_0(k,i\omega_n) &= -\int_0^\beta \mathrm{d}\tau \left(1 - \frac{1}{e^{\beta(\varepsilon_k-\mu)}+1}\right) e^{i\omega_n\tau} e^{-(\varepsilon_k-\mu)\tau} = \ldots =\\ &= \frac{1}{i\omega_n - \varepsilon_k + \mu}.\end{aligned}$$

The Matsubara Green's function of the non-interacting Hamiltonian H_0 is therefore $\mathcal{G}_0(k,i\omega_n) = 1/(i\omega_n - \varepsilon_k + \mu)$. For a system with an interaction term in the Hamiltonian one only has to add the self-energy $\Sigma(k,i\omega_n)$:

$$\mathcal{G}(k,i\omega_n) = \frac{1}{i\omega_n - \varepsilon_k + \mu - \Sigma(k,i\omega_n)}. \tag{2.8}$$

In other words, the contribution of the interaction only enters through the self-energy for the interaction Green's function (this equation can also be written on the form $\mathcal{G}(k,i\omega_n) = (\mathcal{G}_0(k,i\omega_n)^{-1} - \Sigma(k,i\omega_n))^{-1}$). This fact was shown by F.J. Dyson [9] when he expressed the relation between the non-interacting and interacting Green's functions in terms of the self-energy.

Let us return to the non-interacting Hamiltonian and calculate the spectral function using the fact that we already know $\mathcal{G}_0$. The spectral function is given by

$$\begin{aligned} A_0(k,\omega) &= i\left[\mathcal{G}_0(k,\omega+i\eta) - \mathcal{G}_0(k,\omega-i\eta)\right] = \\ &= i\left[\frac{1}{\omega+i\eta-\varepsilon_k+\mu} - \frac{1}{\omega-i\eta-\varepsilon_k+\mu}\right] = \\ &= 2\pi\delta(\omega-\varepsilon_k+\mu). \end{aligned}$$

In other words, for a system describing free electrons the spectral function is just a delta function.

The definitions that were introduced and the properties that we determined in this chapter will not only be used for calculating relevant properties but will also make it easier to understand and interpret the results.

Part I

3 Analytic Continuation

A major difficulty with analytic continuation is that the value of the analytic continuation on the real axis are very sensitive to the values used to determine the function on the complex axis. This is a well known problem for all methods involving analytic continuation. In our case, we will be using Padé approximation to do the analytic continuation, where these instabilities can be monitored using arbitrary precision arithmetic.

In the end of part I we will discuss the stability of the analytic continuation. We also hope to find a relation between the precision of the output and the precision of the input; it will then be possible to decide the accuracy of the input if a certain accuracy of the output is required.

We start by going through the algorithms for the analytic continuation in this chapter and in the next chapter the Jacobian will be determined and compared with the real stability using small noise in the input.

The Green's function of imaginary frequencies is easy to calculate from the spectral function, $A(\omega)$, by using the formula (2.5),

$$G(i\omega_n) = \int \frac{\mathrm{d}\omega}{2\pi} \frac{A(\omega)}{i\omega_n - \omega}, \tag{3.1}$$

where ω_n are the Matsubara frequencies. Since we only know the values of the Green's functions on a finite set of points on the imaginary axis an approximation method will be used, called the Padé method. The Padé fitting gives the Green's function of the whole complex ω-plane.

From many-particle physics one can prove using the spectral representation of Matsubara Green's function that [7]

$$G(i\omega_n) \to \frac{1}{i\omega_n} \text{ when } i\omega_n \to \infty,$$

which means that our Padé approximation should have the form [10]

$$G(z) = \frac{P(z)}{Q(z)} = \frac{p_0 + p_1 z + p_2 z^2 + \ldots + p_{n/2-1} z^{n/2-1}}{1 + q_1 z + q_2 z^2 + \ldots + q_{n/2} z^{n/2}}, \tag{3.2}$$

where $\{p_i\}_{i=0}^{n/2-1}$ and $\{q_i\}_{i=1}^{n/2}$ are unknown coefficients and n is the number of known Matsubara frequencies. The function $G(z)$ denotes the Green's function in the complex plane. When rearranging the factors in (3.2) and

inserting the n different Matsubara frequencies one obtains these equations:

$$\begin{aligned} G(i\omega_1)(1+\ldots+(i)^{n/2}q_{n/2}\omega_1^{n/2}) &= p_0+\ldots+(i)^{n/2-1}p_{n/2-1}\omega_1^{n/2-1} \\ G(i\omega_2)(1+\ldots+(i)^{n/2}q_{n/2}\omega_2^{n/2}) &= p_0+\ldots+(i)^{n/2-1}p_{n/2-1}\omega_2^{n/2-1} \\ &\vdots \\ G(i\omega_n)(1+\ldots+(i)^{n/2}q_{n/2}\omega_n^{n/2}) &= p_0+\ldots+(i)^{n/2-1}p_{n/2-1}\omega_n^{n/2-1} \end{aligned} \tag{3.3}$$

The unknown complex constants $\{p_i\}_{i=0}^{n/2-1}$ and $\{q_i\}_{i=1}^{n/2}$ are easily computed by rewriting (3.3) into a linear equation:

$$\begin{pmatrix} i\omega_1 G(i\omega_1) & \cdots & -1 & \cdots & -(i)^{n/2-1}\omega_1^{n/2-1} \\ i\omega_2 G(i\omega_2) & \cdots & -1 & \cdots & -(i)^{n/2-1}\omega_2^{n/2-1} \\ \vdots & & \vdots & \vdots & \vdots \\ i\omega_n G(i\omega_n) & \cdots & -1 & \cdots & -(i)^{n/2-1}\omega_n^{n/2-1} \end{pmatrix} \begin{pmatrix} q_1 \\ \vdots \\ q_{n/2} \\ p_0 \\ \vdots \\ p_{n/2-1} \end{pmatrix} = - \begin{pmatrix} G(i\omega_1) \\ \vdots \\ G(i\omega_n) \end{pmatrix}$$

$$\Rightarrow \hat{A}\mathbf{x} = -\mathbf{G_n}.$$

Solving these equations gives us the function $G(z) = \frac{P(z)}{Q(z)}$ for any complex number z. The Green's function for the whole real axis (i.e. for real frequencies ω) is obtained by letting z only attain real values.

This procedure of transforming a function of pure imaginary frequencies to the same function of real values achieves the analytic continuation. To check how accurate this method is one can, for known $G(\omega)$, calculate the spectral function using

$$A(\omega) = -2\mathrm{Im}(G(\omega)),$$

and then compare this with the spectral function in (3.1). First a test spectral function has to be defined; we will use a spectral function of a real physical system.

We choose spectral function of a single-site Anderson impurity model in the absence of Coulomb interactions. The system is a one-dimensional, infinite tight-binding lattice with a single impurity at site $i = 0$ (See Fig. 3.1), and is assumed to have zero chemical potential and to be in thermal equilibrium. To find the spectral function for this system we will start with the Hamiltonian that governs the tight-binding geometry:

$$H = -t\sum_i (c_{i+1}^\dagger c_i + c_i^\dagger c_{i+1}) + \varepsilon_0 c_0^\dagger c_0. \tag{3.4}$$

Here $t > 0$ is the hopping amplitude between nearest neighbours, and the impurity located at site $i = 0$ has the strength ε_0, which we assume is

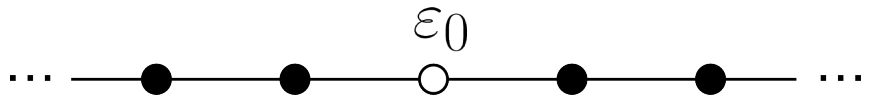

Figure 3.1. *An infinite chain with one impurity at site $i = 0$ and with the hopping amplitude t.*

greater than zero. To compute the spectral function, one needs to find the non-interaction Green's function, G_0, with respect to the first site, $i = 0$. Normally one would calculate the eigenstates and the eigenvalues of the Hamiltonian, but because of the impurity in our problem another approach will be used. First the Green's function of a semi-infinite chain without impurity is calculated with induction. The sought Green's function can then be computed by connecting one impurity site, ε_0, with two baths, for which the Green's function is known as shown in Fig. 3.2.

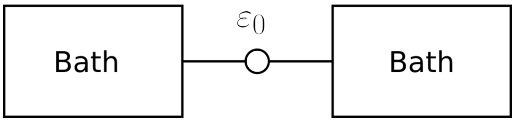

Figure 3.2. *Instead of an infinite chain with impurity, the same system can be seen as two baths connected to the impurity.*

We rewrite the Hamiltonian in (3.4) in a more suitable form:

$$H = \varepsilon_0 c_0^\dagger c_0 - t(c_1^\dagger c_0 + c_0^\dagger c_1) - t(c_0^\dagger c_{-1} + c_{-1}^\dagger c_0) \\ - t\sum_{i=1}^{\infty}(c_{i+1}^\dagger c_i + c_i^\dagger c_{i+1}) - t\sum_{i=-1}^{-\infty}(c_i^\dagger c_{i-1} + c_{i-1}^\dagger c_i)$$

The full Hamiltonian can be presented in block form [11]

$$H = \begin{pmatrix} H_{\alpha',\alpha} & H_{\alpha',0} & \mathbf{0} \\ H_{0,\alpha'} & H_{0,0} & H_{0,\beta} \\ \mathbf{0} & H_{\beta',0} & H_{\beta',\beta} \end{pmatrix},$$

where α', $\alpha = -1, -2\ldots$, β', $\beta = 1{,}2\ldots$ and $\mathbf{0}$ is a block matrix. We know that the Hamiltonians have to fulfill $H_{\alpha',0} = H_{0,\alpha}^T$ and $H_{\beta',0} = H_{0,\beta}^T$.

The matrix Green's function G is obtained by the relation $(zI - H)G = I$;

$$\begin{pmatrix} z\delta_{\alpha',\alpha} - H_{\alpha',\alpha} & H_{\alpha',0} & \mathbf{0} \\ H_{0,\alpha'} & z - H_{0,0} & H_{0,\beta} \\ \mathbf{0} & H_{\beta',0} & z\delta_{\beta',\beta} - H_{\beta',\beta} \end{pmatrix} \begin{pmatrix} G_{\alpha,\alpha''} & G_{\alpha,0} & \mathbf{0} \\ G_{0,\alpha''} & G_{0,0} & G_{0,\beta''} \\ \mathbf{0} & G_{\beta,0} & G_{\beta,\beta''} \end{pmatrix} = I,$$

where $G_{\alpha,\alpha''}$, $G_{\alpha,0}$, $G_{0,\alpha''}$, $G_{0,0}$, $G_{0,\beta''}$, $G_{\beta,0}$ and $G_{\beta,\beta''}$ are the Green's functions corresponding to the Hamiltonians $H_{\alpha',\alpha}$, $H_{\alpha',0}$, $H_{0,\alpha'}$, $H_{0,0}$, $H_{0,\beta}$, $H_{\beta',0}$

and $H_{\beta',\beta}$, respectively and where summation is implied in the repeated submatrix index. The next step is to calculate $\langle 0|(zI-H)^{-1}|0\rangle$, which is done by first studying a more general case. Let A_{ij} and B_{ij} be block matrices,

$$\begin{pmatrix} A_{11} & A_{12} & 0 \\ A_{21} & A_{22} & A_{23} \\ 0 & A_{32} & A_{33} \end{pmatrix} \begin{pmatrix} B_{11} & B_{12} & 0 \\ B_{21} & B_{22} & B_{23} \\ 0 & B_{32} & B_{33} \end{pmatrix} = I.$$

Since we want to find B_{22}, the sought equations are

$$\begin{cases} A_{11}B_{12} + A_{12}B_{22} = 0 & \Rightarrow \quad B_{12} = -A_{11}^{-1}A_{12}B_{22} \\ A_{21}B_{12} + A_{22}B_{22} + A_{23}B_{32} = I & \\ A_{33}B_{32} + A_{32}B_{22} = 0 & \Rightarrow \quad B_{32} = -A_{33}^{-1}A_{32}B_{22} \end{cases}$$

$$\Rightarrow (-A_{21}A_{11}^{-1}A_{12} + A_{22} - A_{23}A_{33}^{-1}A_{32})B_{22} = I.$$

The Green's function G_0 is given by

$$G_0(z) = \langle 0|(zI-H)^{-1}|0\rangle.$$

Using the result in the previous equation and identifying $(A_{21})_{0,\alpha} = H_{0,\alpha}$, $(A_{12})_{\alpha',0} = H_{\alpha',0}$, $(A_{11})_{\alpha',\alpha} = z\delta_{\alpha',\alpha} - H_{\alpha',\alpha}$, $A_{22} = (z-\varepsilon_0)$ etc., and using the fact that the off-diagonal elements of H are just equal to t, we find

$$G_0(z) = \left(-t^2 G_{-1,-1} + z - \varepsilon_0 - t^2 G_{1,1}\right)^{-1}, \tag{3.5}$$

where the Green's function $G_{-1,-1}$ and $G_{1,1}$ are not a block matrix but the Green's function of a semi-infinite chain without impurity at the site $i=-1$ and $i=1$, respectively. The Green's functions $G_{-1,-1}$ and $G_{1,1}$ are describing the same system and are therefore equal, $G_{1,1} = G_{-1,-1} = G'$.

Now that we have an expression relating $G_0(z)$ and the Green's function of the bath, we calculate G' by finding the Green's function for the first site, $i=1$, which will depend on the Green's function G'' for the second site $i=2$ (See Fig. 3.3). As both Green's functions describe a semi-infinite chain they should be equal [12]. The Hamiltonian corresponding to the first site of the

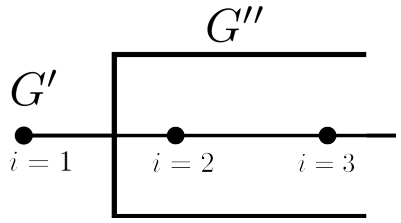

Figure 3.3. *The Green's function G' can be expressed in terms of G''.*

bath is given by

$$H_{\beta',\beta} = -t(c_2^\dagger c_1 + c_1^\dagger c_2) - t\sum_{i=2}^{\infty}(c_{i+1}^\dagger c_i + c_i^\dagger c_{i+1}).$$

Using the same algorithm as before and the fact that $G' = G''$, the equation

$$\begin{pmatrix} z & H_{1,\gamma} \\ H_{\gamma',1} & zI - H_{\gamma',\gamma} \end{pmatrix} \begin{pmatrix} G' & G_{1,\gamma'} \\ G_{\gamma,1} & G_{\gamma,\gamma'} \end{pmatrix} = I$$

becomes

$$G' = \frac{1}{z - t^2 G'} \Rightarrow G'(z) = \frac{z \pm \sqrt{z^2 - 4t^2}}{2t^2}.$$

The Green's function for an infinite chain with impurity is therefore given by

$$G_0(z) = \left(z - \varepsilon_0 - 2t^2 G'(z)\right)^{-1} = \left(-\varepsilon_0 \pm \sqrt{z^2 - 4t^2}\right)^{-1}. \tag{3.6}$$

The spectral function has to be positive, so one only needs to consider one of the solutions (when $\mathrm{Im}G_0 < 0$). The Green's function can then be written as

$$G_0(z) = \begin{cases} \frac{1}{-\varepsilon_0 + i\sqrt{4t^2 - z^2}} & |z| \leq 2t \\ \frac{1}{-\varepsilon_0 + \sqrt{z^2 - 4t^2}} & |z| > 2t \end{cases}$$

In the case $|z| > 2t$, there is a singularity at $\sqrt{z^2 - 4t^2} = \varepsilon_0$ that can be avoided by using the substitution $z = \omega + i\eta$, for $\eta \to 0$. The Green's function for $|z| > 2t$ is

$$\begin{aligned} \frac{1}{-\varepsilon_0 + \sqrt{(\omega + i\eta)^2 - 4t^2}} &= \frac{1}{-\varepsilon_0 + \sqrt{\omega^2 - 4t^2}\sqrt{1 + \frac{2i\omega\eta}{\omega^2 - 4t^2}}} \\ &= \frac{1}{-\varepsilon_0 + i\eta' + \sqrt{\omega^2 - 4t^2}}, \end{aligned}$$

where $\eta' = i\omega\eta/(\omega^2 - 4t^2) \to 0$ when $\eta \to 0$. So the Green's function in terms of frequency ω is:

$$G_0(\omega) = \begin{cases} \frac{1}{-\varepsilon_0 \pm i\sqrt{4t^2 - \omega^2}} & |\omega| \leq 2t \\ \frac{1}{-\varepsilon_0 + i\eta' \pm \sqrt{\omega^2 - 4t^2}} & |\omega| > 2t \end{cases}$$

Thus, the spectral function $A(\omega)$ is given by

$$\begin{aligned} A(\omega) =& \frac{1}{\pi} \frac{\sqrt{4t^2 - \omega^2}}{4t^2 - \omega^2 + \varepsilon_0^2} \theta(|\omega| - 2t) \\ &+ \frac{\varepsilon_0}{\sqrt{4t^2 + \varepsilon_0^2}} \delta(\omega - \sqrt{4t^2 + \varepsilon_0^2}), \end{aligned}$$

where we have rewritten the delta function using the relation $\delta(f(x)) = \sum_i \delta(x - x_i)/|\frac{df}{dx}(x_i)|$, and $\eta' \to 0$. In this thesis we choose $t = 1$ and $\varepsilon_0 = 1.5$ as in [13], which gives us the expression

$$A(\omega) = \frac{1}{\pi} \frac{\sqrt{4 - \omega^2}}{6.25 - \omega^2} \theta(|\omega| - 2) + \frac{3}{5} \delta(\omega - 2.5). \tag{3.7}$$

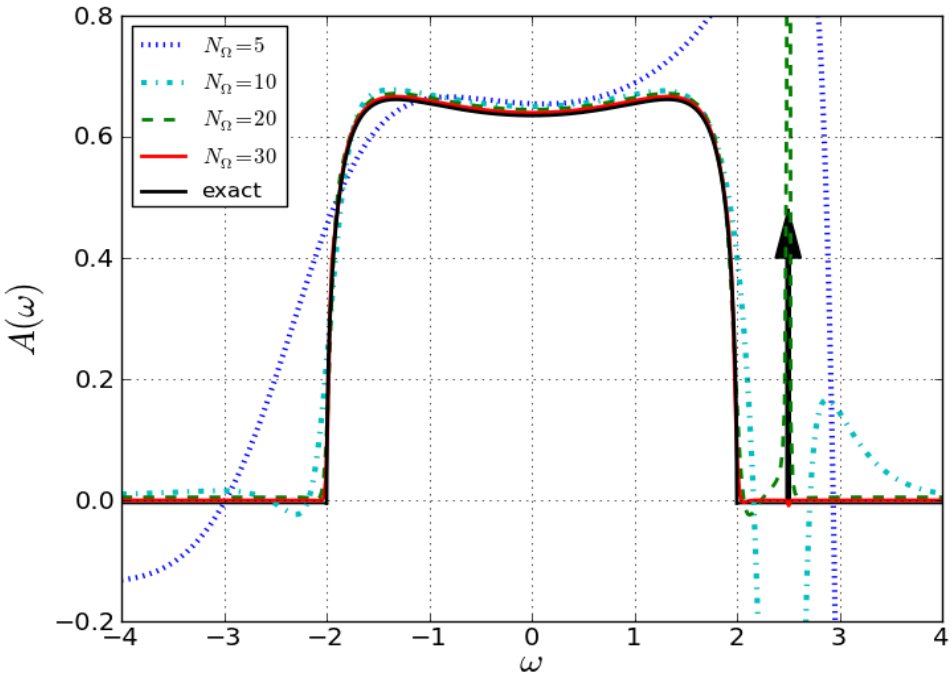

Figure 3.4. *The spectral function after analytic continuation when using different N_Ω, together with the spectral function before performing the analytic continuation ("exact" line).*

Now, let us use this spectral function to analyze the analytic continuation. A crucial thing is that the accuracy of the analytic continuation depends on how many Matsubara frequencies N_Ω are used: a higher value of N_Ω means higher order of $P(z)$ and $Q(z)$ which gives a more accurate approximation of the Green's function of real values. In Fig. 3.4 the spectral function given in (3.7) is plotted together with spectral functions computed with analytic continuation for different N_Ω.

For $N_\Omega \approx 20$ the approximated spectral function is almost the same as (3.7). Hence, when investigating this analytic continuation, $N_\Omega > 20$ will be used from now on.

4 Stability of the Analytic Continuation

We are interested in investigating the analytic continuation to the real axis of a function whose values are $\{G_i\}_{i=1}^n \equiv \{G(i\omega_i)\}_{i=1}^n$ on the imaginary axis. We want to know the values $\{G_j^r\}_{j=1}^m \equiv \{G(x_j)\}_{j=1}^m$ on the real axis. Since the analytic continuation is defined only by a discrete set of values, the analytic continuation is not unique, and the stability of the results may depend on the choice of form for the analytic continuation. In our case, we will let the Padé approximation determine the analytic continuation and we will discuss the stability of this continuation scheme as a function of the values on the imaginary axis.

We define $\mathbb{F}(\boldsymbol{G})$ to be a function of input values $\boldsymbol{G}$. $\mathbb{F}$ then calculates an analytic continuation based on these values and gives $\boldsymbol{G}^r$ corresponding to a set of argument on the real axis. Thus we may write

$$\mathbb{F} : \boldsymbol{G} \underset{\mathbb{F}_1}{\mapsto} (\alpha_1 \dots \alpha_n) \underset{\mathbb{F}_2}{\mapsto} \boldsymbol{G}^r$$

where $(\alpha_1 \dots \alpha_n)$ are parameters parameterizing our analytic continuation in (3.2). In our case $(\alpha_1, \cdots, \alpha_{n/2}, \alpha_{n/2+1}, \cdots, \alpha_n) = (p_0, \cdots, p_{n/2-1}, q_1, \cdots, q_{n/2})$, where p and q are the coefficients of the Padé fit to $\boldsymbol{G}$. With this notation we have $\mathbb{F} = \mathbb{F}_2 \circ \mathbb{F}_1$.

The Jacobian of this transormation is given by

$$\frac{\partial \mathbb{F}(\boldsymbol{G})}{\partial \boldsymbol{G}} = J$$

Since $\mathbb{F} = \mathbb{F}_2 \circ \mathbb{F}_1$ we know that $J = J_2 J_1$ where each of these Jacobians are given by

$$(J_1)^{-1} = \begin{pmatrix} \frac{\partial G_1}{\partial \alpha_1} & \frac{\partial G_1}{\partial \alpha_2} & \cdots & \frac{\partial G_1}{\partial \alpha_n} \\ \frac{\partial G_2}{\partial \alpha_1} & \frac{\partial G_2}{\partial \alpha_2} & \cdots & \frac{\partial G_2}{\partial \alpha_n} \\ \vdots & \vdots & \ddots & \vdots \\ \frac{\partial G_n}{\partial \alpha_1} & \frac{\partial G_n}{\partial \alpha_2} & \cdots & \frac{\partial G_n}{\partial \alpha_n} \end{pmatrix},$$

where we have utilized the fact that the Jacobian transformation of the inverse function is given by the inverse Jacobian and G_j is given by (3.2). The second part, J_2, will be the Jacobian of the mapping going from the

space α of Padé coefficients to $\boldsymbol{G}^r$:

$$J_2 = \begin{pmatrix} \frac{\partial G_1^r}{\partial \alpha_1} & \frac{\partial G_1^r}{\partial \alpha_2} & \cdots & \frac{\partial G_1^r}{\partial \alpha_n} \\ \frac{\partial G_2^r}{\partial \alpha_1} & \frac{\partial G_2^r}{\partial \alpha_2} & \cdots & \frac{\partial G_2^r}{\partial \alpha_n} \\ \vdots & \vdots & \ddots & \vdots \\ \frac{\partial G_m^r}{\partial \alpha_1} & \frac{\partial G_m^r}{\partial \alpha_2} & \cdots & \frac{\partial G_m^r}{\partial \alpha_n} \end{pmatrix},$$

The Jacobian J_2 is therefore not necessarily a square matrix. It is important to stress that arbitrary precision arithmetic has to be used to enable the numerical calculation of J.

In order to investigate the stability of this mapping, we look at the numerical difference on the real axis obtained by varying the input data on the imaginary axis. Thus we define $\delta\mathbb{F} = \mathbb{F}(\boldsymbol{G} - \boldsymbol{\delta}) - \mathbb{F}(\boldsymbol{G})$ and $\boldsymbol{\delta}$ is some small noise applied invidually to each of the input values along the imaginary axis. The question we would like to address is what the limit to the noise must be so that the deviation is approximated by a linear tranformation:

$$\delta\mathbb{F} \approx J\boldsymbol{\delta}. \tag{4.1}$$

Let us now see to what extent the approximation holds for different noise levels. In Fig. 4.1 one can see $\delta\mathbb{F}$ for $N_\Omega = 32, 40, 52, 60$ when $||\boldsymbol{\delta}|| = \delta = 10^{-10}, 10^{-20}, 10^{-30}, 10^{-40}, 10^{-50}, 10^{-80}, 10^{-90}, 10^{-130}$, i.e. the left hand side of equation (4.1) is plotted.

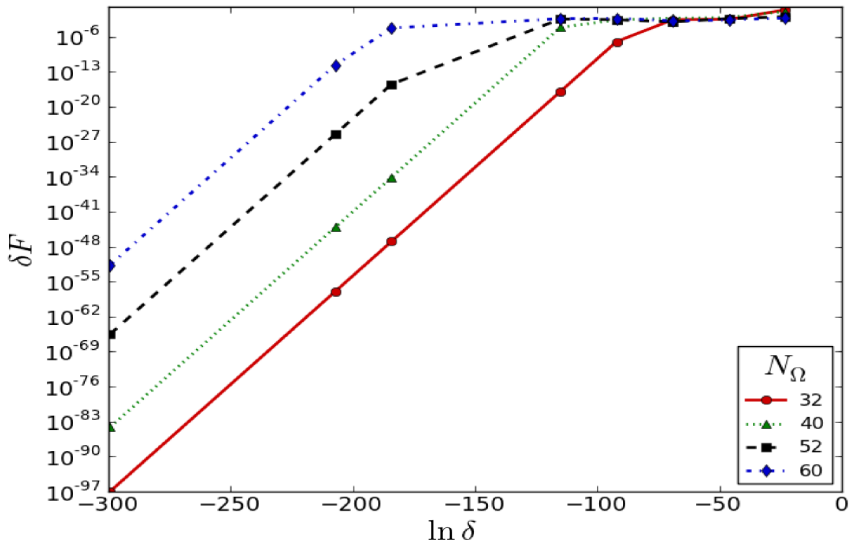

Figure 4.1. *The error δF as a function of the noise δ when using different values of N_Ω.*

For small noise levels δ the error of the function $\mathbb{F}$ increases for larger values of N_Ω, and after a certain threshold the slope of the graph decreases so that for large magnitudes of δ the function $\mathbb{F}$ gives the same error for different values of N_Ω. From Fig. 4.1 one can learn that if $N_\Omega = 32$ and an accuracy of twenty decimal places on the output data is needed, the input data must have a precision of at least fifty decimal places.

It is perhaps not intuitive that a function $\mathbb{F}$, which is unstable for small noise levels, starts to be very stable for larger values of δ. The reason why $\mathbb{F}$ is unstable for small values of δ should be because the poles in $G(z)$, i.e. the roots of $Q(z)$, are moved when some noise δ is added. Even small displacements of the poles give large differences for values close to the poles. A relevant question is then; why does the Fig. 4.1 have a breaking point where the slope of the curve decreases? Most of the first part of the thesis will focus on explaining this behavior.

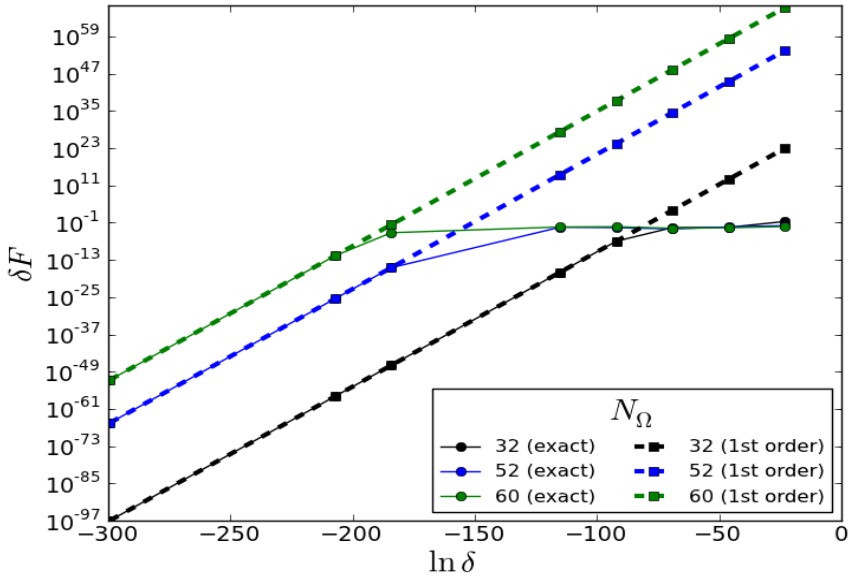

Figure 4.2. *The first order approximation of the analytic continuation for different values of N_Ω, together with the error $\delta\mathbb{F}$.*

In Fig. 4.2 the first order approximation (the right hand side of (4.1)) is visualized together with the exact error $\delta\mathbb{F}$. The figure shows that (4.1) is only satisfied for small δ, where the breaking point is not reached. It is evident from both Fig. 4.1 and Fig. 4.2 that the breaking point depends on N_Ω.

It is worth mentioning that the error also depends on which interval of the real axis is considered. If we choose points near the poles the error of $\mathbb{F}$ increases. In these plots we have chosen to consider points in the interval

$\omega \in [-5,5]$ where our spectral function $A(\omega) \neq 0$. In Fig. 4.2 we only change the value of N_Ω and the number of values on the real axis is kept constant. The reason for this is that the value of N_r does not affect the stability, which is shown in the next section.

Using singular value decomposition the Jacobian may be written as

$$J = U\Sigma V^T = \sum_j \lambda_j \boldsymbol{u}_j \boldsymbol{v}_j^T, \tag{4.2}$$

where $\boldsymbol{u_j}$ and $\boldsymbol{v_j}$ are the left and right eigenvectors, respectively, of the Jacobian, and λ_j are the singular values. One may reason, using this form of the Jacobian, that the direction that contributes the most to the first order approximation of $\mathbb{F}$ is the eigenvector, $\boldsymbol{u}_{\max}$, corresponding to the largest singular value $\lambda_{\max}$. In order to verify this, the values of $\delta\mathbb{F} = \mathbb{F}(\boldsymbol{G} + \boldsymbol{\delta}) - \mathbb{F}(\boldsymbol{G})$ is plotted and compared with the first order Taylor expansion and we use $\boldsymbol{\delta} = \delta \boldsymbol{u}_{\max}$ in Fig. 4.3. The figure shows that the first order Taylor expansion has a slope with the same magnitude as $\lambda_{\max}\delta\boldsymbol{u}_{\max}$. Hence, we can conclude that the maximum eigenvector contributes the most to the Jacobian, which means that it is not necessary to take the other terms into account. We will later use this fact to calculate the second order Taylor expansion of the transformation $\mathbb{F}$.

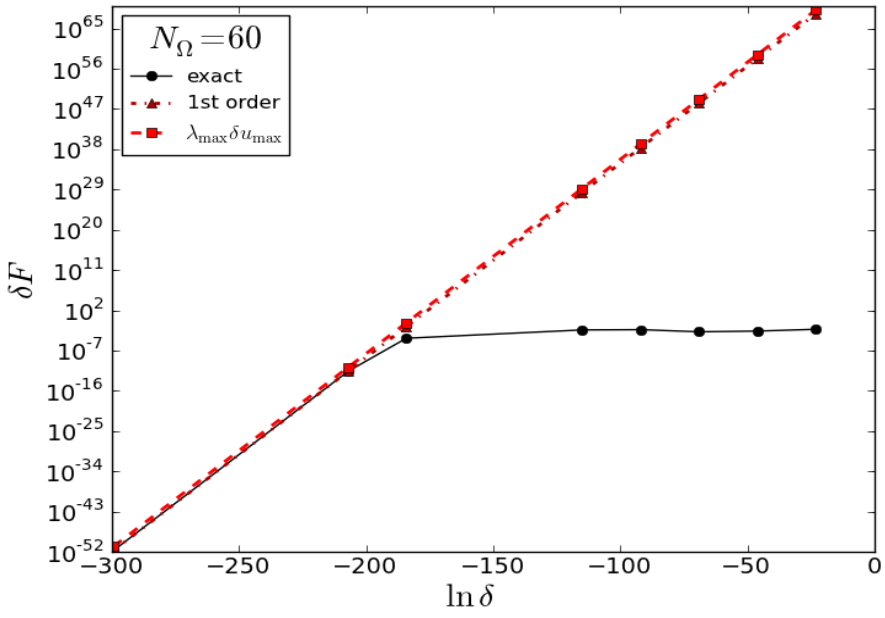

Figure 4.3. *The "exact" error $\delta\mathbb{F}$ and the first order approximation $J\boldsymbol{\delta}$, together with the function $\lambda_{\max}\delta\boldsymbol{u}_{\max}$. N_Ω is set to a constant value.*

4.1 Singular Values of the Jacobian

The Jacobian is now investigated to see how the number of points on the imaginary axis, N_Ω, and the number of points on the real axis, N_r, affect the singular values of the Jacobian, and if it is possible to find a dependence on N_Ω and N_r. If this is shown to be true then we only need to consider one case and the rest can be calculated through scaling. It is especially important to investigate whether the maximum singular value, $\lambda_{\max}$, depends on N_Ω and N_r, because it is the term of the Jacobian that contributes most to the error.

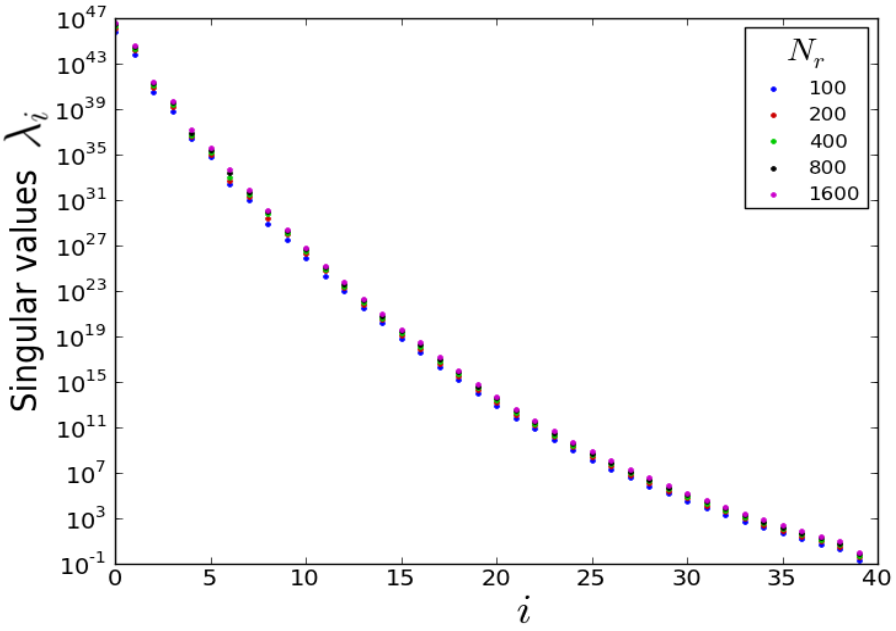

Figure 4.4. *The singular values of the Jacobian for different values of N_r, when $N_\Omega = 40$.*

The singular values of the Jacobian J can be seen in Fig. 4.4 and Fig. 4.5. In Fig. 4.4 the different lines have different values of N_r, and $N_\Omega = 40$, while N_Ω is varying and N_r is constant in Fig. 4.5. In both cases the difference between $\lambda_{\max}$ and $\lambda_{\min}$ is huge, and $\lambda_{\max} \gg \lambda_i$ for $\lambda_i \neq \lambda_{\max}$. This would explain Fig. 4.3 which indicates that the maximum singular value and its corresponding eigenvector is the term that contributes the most in the Jacobian.

In Fig. 4.4 it seems that both the maximum and minimum singular values are constant for all N_r. This becomes clearer in Fig. 4.6 and Fig. 4.7 which show only the maximum and minimum singular values $\lambda_{\max}$ and $\lambda_{\min}$, respectively, for different values of N_r. It seems as if the maximum singular

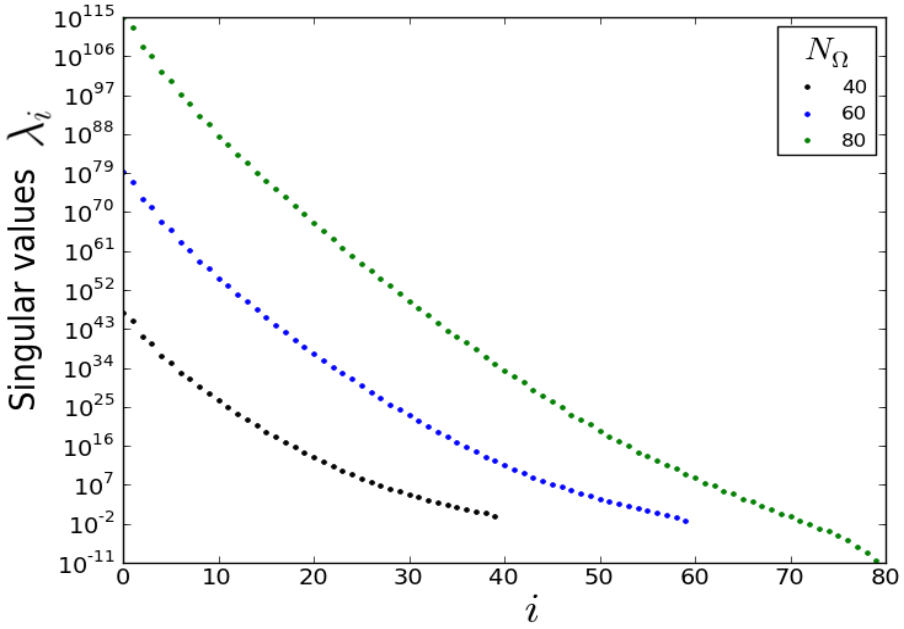

Figure 4.5. *The singular values of the Jacobian when $N_r = 100$ while the number of Matsubara frequencies is varying.*

value does not depend on N_r. This means that the choice of N_r does not change the singularities of J, i.e. the stability is unchanged. Therefore, we do not need to consider N_r, and it will be set to a constant.

The minimum singular value λ_{min}, however, seems to depend on the value of N_r in a way that is difficult to predict.

Fig. 4.8 illustrates the N_Ω-dependence of the singular values of the Jacobian. It is shown that for higher values of N_Ω the maximum singular value increases, while the minimum singular value can be seen to decrease in Fig. 4.9. Fig. 4.8 shows that λ_{max} does not have a linear dependence on N_Ω, and because any other dependence was not possible to find one has to consider different values of N_Ω when investigating the stability, i.e. no scaling can be made.

In the case of Fig. 4.9 it was not possible find any good fitting relating λ_{min} and N_Ω.

In summary, by examining the singular values we learned that the Jacobian is not dependent on N_r. The next step is to add one order to our Taylor expansion of the transformation $\mathbb{F}$ to see if it is possible to explain the behavior of $\delta\mathbb{F}$.

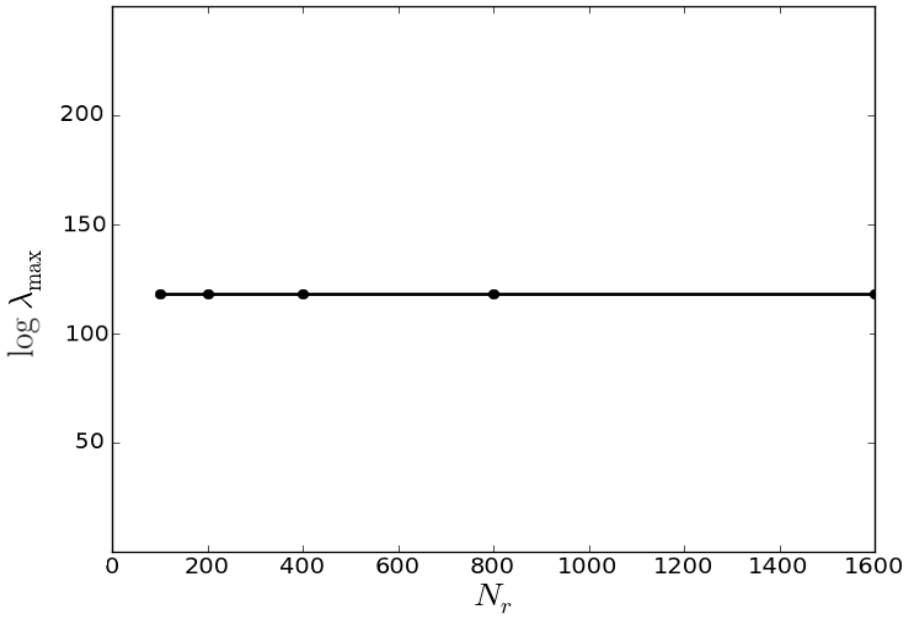

Figure 4.6. *The maximum singular value $\lambda_{\max}$ as a function of N_r. The number of frequencies $N_\Omega = 40$.*

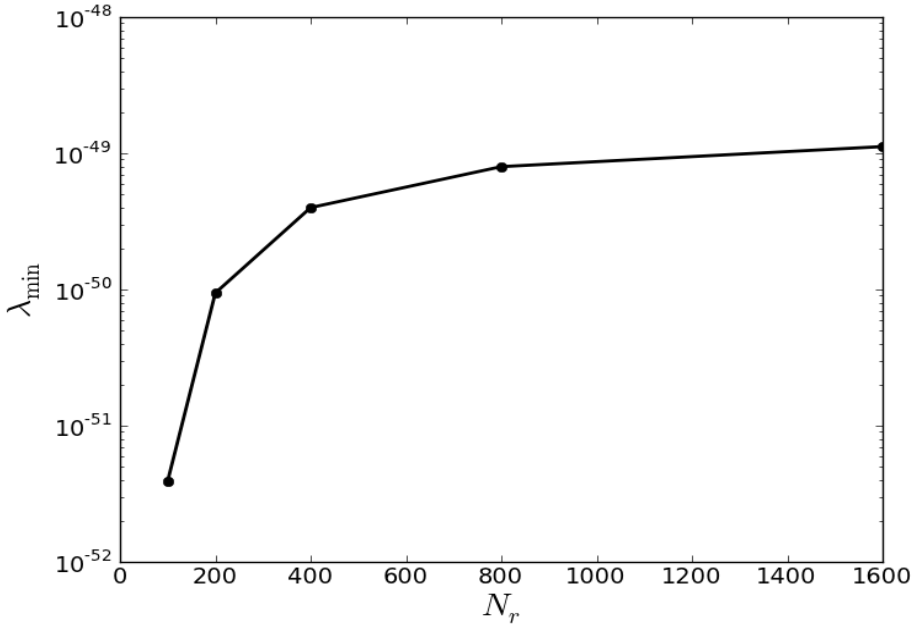

Figure 4.7. *The minimum singular value $\lambda_{\min}$ as a function of N_r. The number of frequencies $N_\Omega = 40$.*

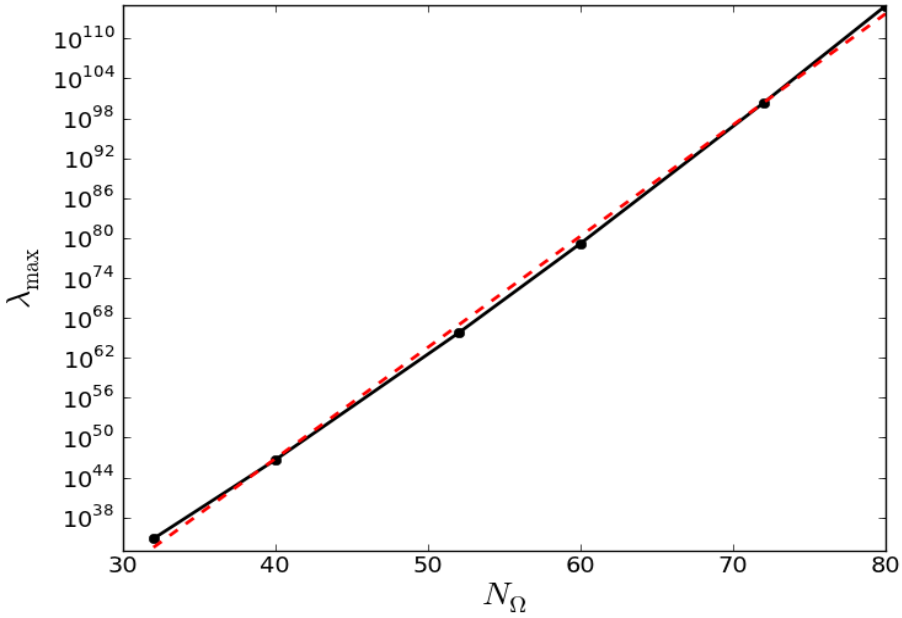

Figure 4.8. *The maximum singular value* $\lambda_{\max}$ *as a function of* N_Ω*. The number of values on the real axis* $N_r = 100$*. The dashed line is a linear fit of* $\log(\lambda_{\max}(N_\Omega))$*.*

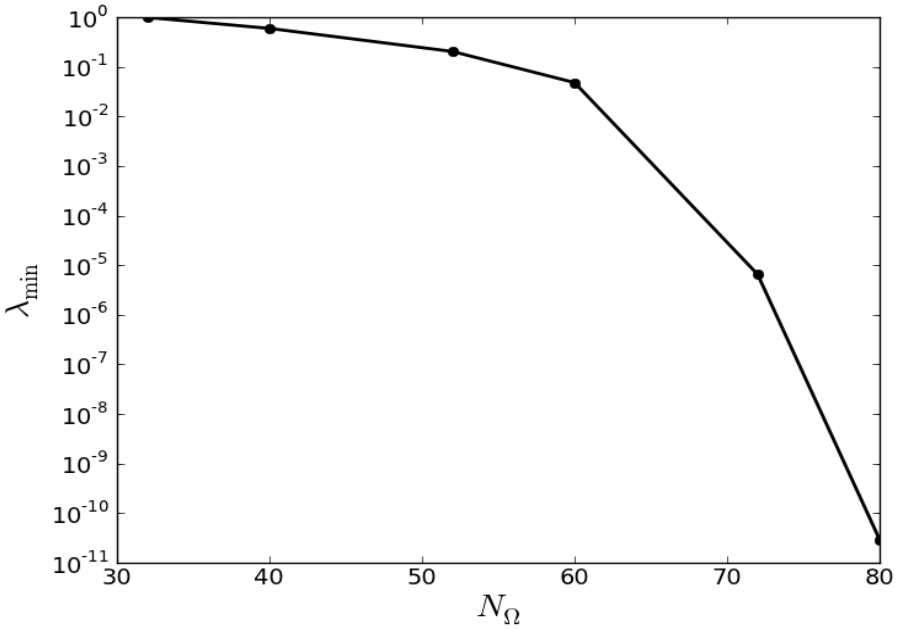

Figure 4.9. *The minimum singular value $\lambda_{\min}$ as a function of N_Ω. The number of values on the real axis $N_r = 100$.*

4.2 Second Order Taylor Expansion

The utilization of the first order Taylor expansion did not provide an explanation as to why there is a breaking point in Fig. 4.2. We will instead try to explain this behavior using the second order. Let us first define $\delta\mathbb{F}$ for the second order Taylor expansion. We do this by adding some noise $\boldsymbol{\delta}$ to $\boldsymbol{G}$, plug the result into $\mathbb{F}$ and apply Taylor expansion like so:

$$\begin{aligned}
\mathbb{F}(\boldsymbol{G}+\boldsymbol{\delta}) &\approx \mathbb{F}(\boldsymbol{G}) + \frac{\partial\mathbb{F}(\boldsymbol{G})}{\partial G_i}\delta_i + \frac{\partial^2\mathbb{F}(\boldsymbol{G})}{\partial G_i \partial G_j}\delta_i\delta_j, \\
\mathbb{F}(\boldsymbol{G}+\boldsymbol{\delta}) - \mathbb{F}(\boldsymbol{G}) &\approx \frac{\partial\mathbb{F}(\boldsymbol{G})}{\partial G_i}\delta_i + \frac{\partial^2\mathbb{F}(\boldsymbol{G})}{\partial G_i \partial G_j}\delta_i\delta_j, \\
\delta\mathbb{F} &\approx \frac{\partial\mathbb{F}(\boldsymbol{G})}{\partial G_i}\delta_i + \frac{\partial^2\mathbb{F}(\boldsymbol{G})}{\partial G_i \partial G_j}\delta_i\delta_j.
\end{aligned}$$

Calculating the second order term can be very computationally intense. However, we expect the error to be dominated by noise projected into the dominate eigenvector of J. Therefore we choose to numerically evaluate the second order contribution in this direction by using $\delta_i = \delta(\boldsymbol{u}_{\max})$:

$$\frac{\partial^2\mathbb{F}(\boldsymbol{G})}{\partial G_i \partial G_j}\delta_i\delta_j \approx \mathbb{F}(\boldsymbol{G}+\delta\boldsymbol{u}_{\max}) + \mathbb{F}(\boldsymbol{G}-\delta\boldsymbol{u}_{\max}) - 2\mathbb{F}(\boldsymbol{G}) \tag{4.3}$$

where $\delta \boldsymbol{u}_{\max}$ is the error with the same direction as for the eigenvector corresponding to the singular value $\lambda_{\max}$.

The second order approximation is plotted together with the exact error in Fig. 4.10 for $N_\Omega = 32, 52, 60$. We see that there is a breaking point when using the second order and the curve changes direction,

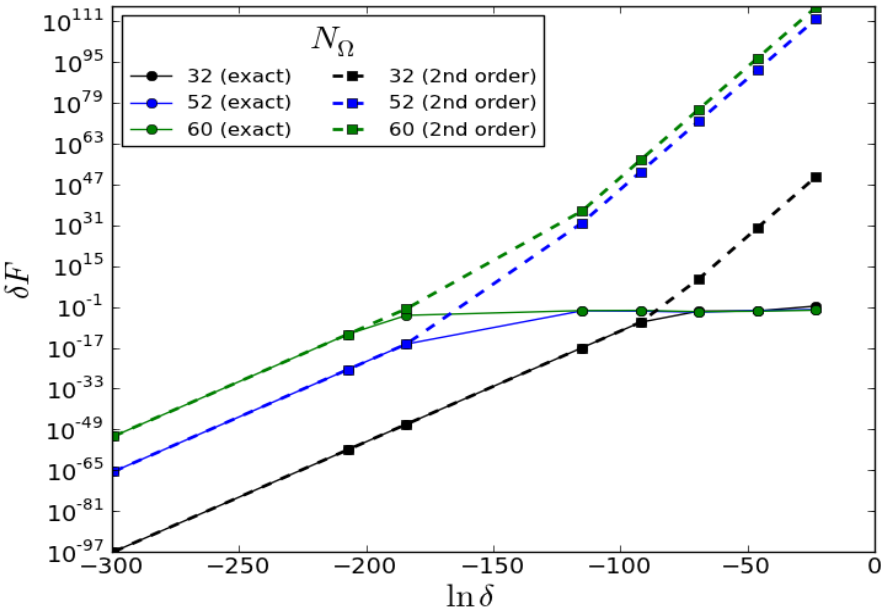

Figure 4.10. *The second order approximation, together with the "exact" error, for different values of* N_Ω.

We will now separate the mapping $\mathbb{F}$ into two parts and examine the error of its different parts separately. The transformation from the imaginary axis to the space α of the Padé coefficient is denoted by $\mathbb{F}_1$, and the transformation from the space α of the Padé coefficient to the real axis is $\mathbb{F}_2$. The errors of both $\mathbb{F}_1$ and $\mathbb{F}_2$ are plotted in Fig. 4.11 together with the whole transformation $\mathbb{F}$ for different noise levels. We can see that the error of $\mathbb{F}_2$ is much less than for $\mathbb{F}$. Surprisingly, $\mathbb{F}_1$ has an error which is larger than the error of $\mathbb{F}$. Fig. 4.12 shows how many times greater the error of $\mathbb{F}_1$ is compared to that of $\mathbb{F}$. The difference in precision between $\mathbb{F}_1$ and $\mathbb{F}$ is not large enough to be able to explain the behavior of Fig. 4.1.

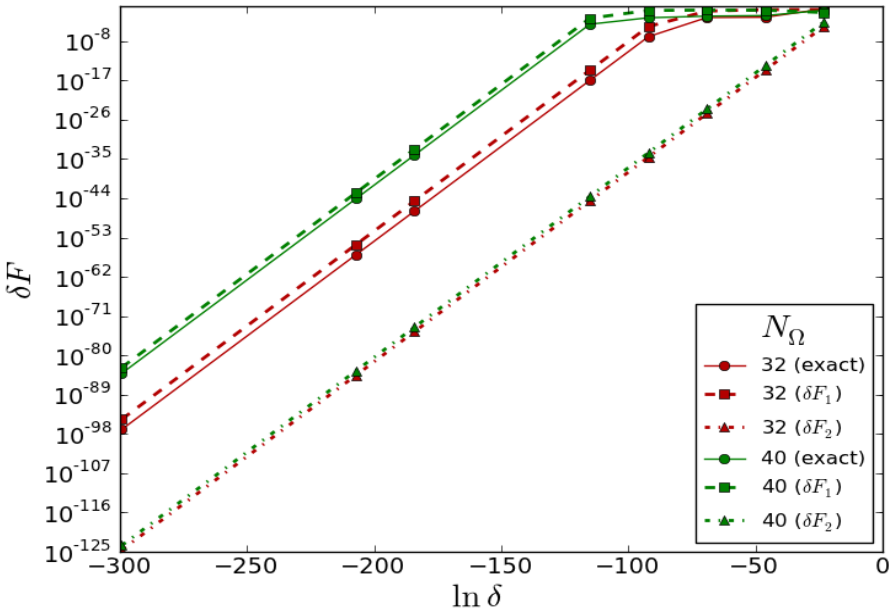

Figure 4.11. *The error $\delta\mathbb{F}$ for the whole transformation $\mathbb{F}$, and the errors $\delta\mathbb{F}_1$ and $\delta\mathbb{F}_2$ for the different parts $\mathbb{F}_1$ and $\mathbb{F}_2$ of the analytic continuation, as functions of the noise level δ.*

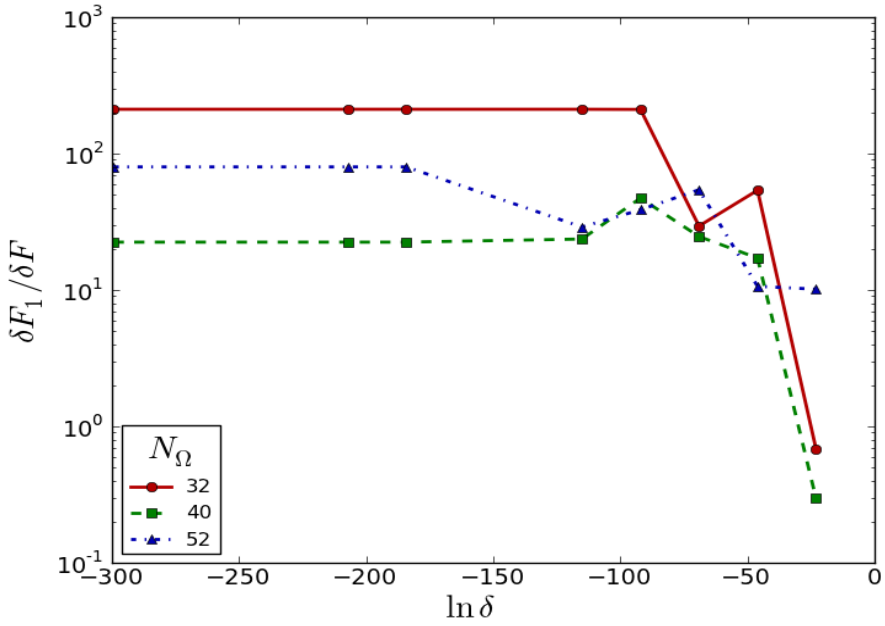

Figure 4.12. *The ratio $\delta\mathbb{F}_1/\delta\mathbb{F}$ as a function of the noise level, for different N_Ω.*

5 Conclusions

As we have seen in Fig. 4.1 the analytic continuation using Padé approximation seems to be unstable for small noise levels. The Green's function on the real axis is highly sensitive to the locations of the poles, which explains why a small increase of the noise leads to a much larger error of the output. However, there is a certain threshold of the noise level, where adding more noise no longer decreases the precision of the output. This is contrary to what is predicted when computing the singular values of the Jacobian; these are large and one would therefore expect non-physical results even for relatively small noise.

The Jacobian can be described by the maximum singular value, $\lambda_{\max}$, and its corresponding eigenvectors. The N_r and N_Ω dependence of $\lambda_{\max}$ was examined, and it was found that the singular value $\lambda_{\max}$ does not depend on N_r but rather on the value of N_Ω. We therefore conclude that one only needs to consider the stability for different values of N_Ω.

The breaking point in Fig. 4.1 can not be described by the second order Taylor expansion of the transformation $\mathbb{F}$. The second order Taylor expansion can explain the linearity for small noise but at the breaking point our approximation becomes even more unstable. The reason why the second order expansion fails to describe the stability of the analytic continuation is probably due to some non-linear behavior of the Padé method that reduces the error.

By investigating the different parts of the analytic continuation one realizes that the error of $\delta\mathbb{F}_1$ is higher than for $\delta\mathbb{F}$, and the precision must therefore be higher when using the analytic continuation than one would expect at first. However the difference is not large and probably does not need to be taken into account.

We were not able to understand why there is a breaking point where the analytic continuation becomes stable, and do not know how to investigate it further.

Part II

6 Dynamical Mean Field Theory

Materials such as iron, vanadium and their oxides, which have strongly interacting electrons that are spatially confined in their orbits around the nucleus, have properties that are hard to explain [4]. The correlation between electrons makes it impossible to treat them independently. These materials are instead described by a simplified Hamiltonian to take into account a few relevant degrees of freedom. One model that will be used in this thesis is the Hubbard model:

$$H = \sum_{ij,\sigma} t_{ij} c^{\dagger}_{i\sigma} c_{j\sigma} + U \sum_{i} n_{i\uparrow} n_{j\downarrow}. \tag{6.1}$$

The Hubbard model assumes interaction of electrons only when they are located at the same lattice site i, with interaction energy U. The equation also describes the kinetic energy of an electron with spin σ hopping between the orbits at lattice sites i and j, and this energy is denoted t_{ij}.

In the Hubbard model only local interactions are considered, and evaluating the self-energy exactly is therefore a fairly difficult task. The problem is simplified through an expansion in the coordinate number z (the number of neighbors) when scaling the kinetic energy as $t \to t/\sqrt{z}$, and this procedure will make DMFT exact in the limit $z \to \infty$. The approximation captures many features of physics in finite dimensions. The scaling causes the total self-energy to be independent of the momentum [14]:

$$\Sigma(\mathrm{k}, i\omega_n) \longrightarrow \Sigma(i\omega_n) \quad \text{as} \quad z \to \infty.$$

Using the fact that $G(\vec{R},i\omega_n) = \sum_{\mathrm{k}} e^{ik\vec{R}} G(\mathrm{k},i\omega_n)$ the local interacting Green's function G_L can now be calculated as

$$G_L(i\omega_n) = \int d\varepsilon \frac{\rho_0(\varepsilon)}{i\omega_n - \varepsilon + \mu - \Sigma(i\omega_n)},$$

where $\rho_0(\varepsilon)$ is the non-interacting density of states and where the Green's function in (2.8) is used.

The lattice problem is mapped to an auxiliary impurity problem (See Fig. 6.1). The local lattice Green's function $G_L(i\omega_n)$, the bath Green's function $G_0(i\omega)$ and the lattice self-energy $\Sigma(i\omega)$ are related by

$$G_0^{-1} = G_L^{-1} + \Sigma. \tag{6.2}$$

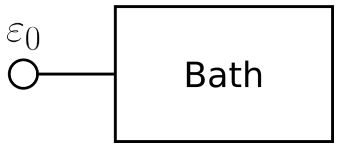

Figure 6.1. *An impurity connected with a bath with Green's function G_0.*

It is important to stress that (6.2) is not the Dyson equation discussed in Chapter 2; it is an additional relation that relates the lattice problem with an impurity problem.

The derivation of the impurity problem and the self-consistency condition is done by first separating the lattice action S into three parts; a lattice with cavity $S^{(0)}$, the cavity S_0 and its connection, ΔS, to the bath [15]:

$$S = S^{(0)} + S_0 + \Delta S.$$

This is also visualized in Fig. 6.2. The derivation of (6.2) is out of scope of this thesis.

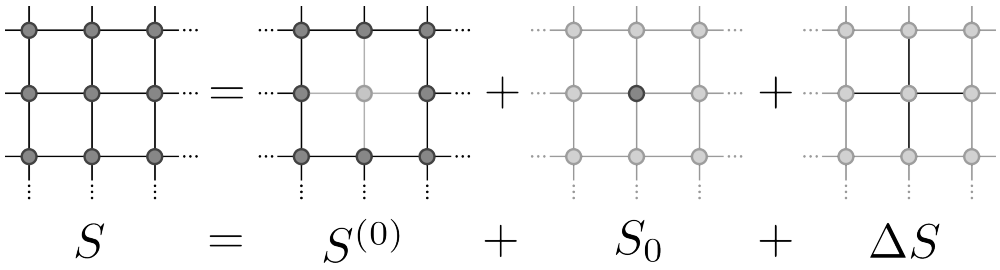

Figure 6.2. *The action of the lattice problem is divided into three parts.*

Now that the effective bath Green's function G_0 of the impurity problem has been derived, the next step is to compute the local interacting Green's function G_I of the impurity, which takes the following form:

$$G_{I\sigma\sigma'} = \int_0^\beta d\tau e^{i\omega_n \tau} \langle c_\sigma(\tau) c^\dagger_{\sigma'}(0) \rangle_{S_{eff}[G_0]}, \tag{6.3}$$

where the effective action of the impurity is

$$\begin{aligned} S_{eff}[G_0] = &\int_0^\beta d\tau U n_\uparrow(\tau) n_\downarrow(\tau) - \\ &- \int_0^\beta d\tau \int_0^\beta d\tau' \sum_\sigma c^\dagger_\sigma(\tau) G_0^{-1}(\tau - \tau') c_\sigma. \end{aligned}$$

The first term $U n_\uparrow(\tau) n_\downarrow(\tau)$ is the local interaction of the lattice.

There are many ways to solve (6.3). Some methods use renormalization group techniques, e.g. numerical renormalization group (NRG) and exact

diagonalization (ED), while some use methods based on the stochastic sampling of quantum and thermal averages, e.g. Hirsch-Fye QMC algorithm and continuous-time (CT) QMC [2],[16]. In this thesis we will focus on exact diagonalization. The first step in exact diagonalization is to map the known impurity bath Green's function G_0 into the Anderson model formulation. Thus, an introduction to the Anderson model is needed.

6.1 Anderson Model Mapping

The Anderson model was introduced 1961 by P.W. Anderson [17] and is an effective model for magnetic impurities in metallic systems. The Anderson model describes one impurity site with energy ε_0 and interaction energy U. The impurity site is coupled by a hybridization V_k to non-interacting sites with the energy ε_k (See Fig. 6.3). The Anderson Hamiltonian takes the form

$$H_{\mathrm{AM}} = \sum_{\sigma}(\varepsilon_0 - \mu)c_\sigma^\dagger c_\sigma + U n_\uparrow n_\downarrow + \sum_{\sigma,k=1}^{\infty}\left(\varepsilon_k c_{k\sigma}^\dagger c_{k\sigma} + V_k(c_\sigma^\dagger c_{k\sigma} + c_{k\sigma}^\dagger c_\sigma)\right), \tag{6.4}$$

where $c_\sigma^\dagger$ and c_σ are the creation and annihilation operators, respectively, at the impurity site. k is a quantum label of the momentum.

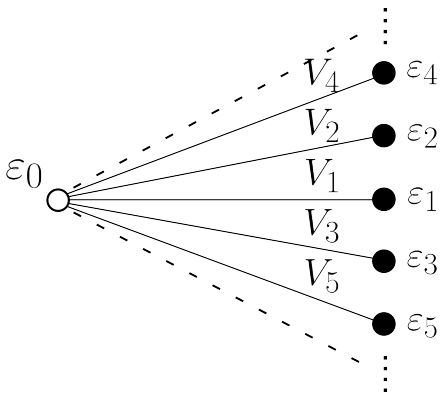

Figure 6.3. *The Anderson model describes an impurity site which is connected to infinitely many non-interacting electron systems.*

When using cavity construction, as in the previous chapter, one obtains a relation between impurity bath Green's function and the Anderson model formulation given by

$$G_0^{-1}(i\omega_n) = i\omega_n + \mu - \varepsilon_0 - \Delta(i\omega_n), \tag{6.5}$$

where $\Delta(i\omega_n)$ is the hybridization function,

$$\Delta(i\omega_n) = \sum_{k=1}^{\infty}\frac{|V_k|^2}{i\omega_n - \varepsilon_k}.$$

Note that when one sums over an infinite number of sites one has an exact mapping between the auxiliary impurity problem and the Anderson model. This is used in the next chapter when applying exact diagonalization to calculate the interacting Green's function G_I in (6.3).

6.2 Exact Diagonalization

In 1993, M. Caffarel and W. Krauth [18] published an article about an exact diagonalization (ED) method to calculate an infinite dimensional Hubbard model by using exact diagonalization of an Anderson model with a finite number of sites. Truncating the Anderson model (6.4) to a finite number of sites gives the Hamiltonian that is used in ED:

$$H^{ED} = (\varepsilon_0 - \mu)\sum_{\sigma} c_\sigma^\dagger c_\sigma + U n_\uparrow n_\downarrow + \sum_{\sigma,i=1}^{n} \left(V_i (c_{i\sigma}^\dagger c_\sigma + h.c.) + \varepsilon_i c_\sigma^\dagger c_\sigma \right).$$

This means that the non-interacting Green's function of the Hubbard model can be approximated through (6.5) to obtain

$$G_0(i\omega_n) \approx G_0^{ED}(i\omega_n) = \left(i\omega_n - \varepsilon_0 + \mu - \sum_{i=1}^{n} \frac{V_i}{i\omega_n - \varepsilon_i} \right)^{-1},$$

where n is the number of sites excluding the local interaction site. However, since a finite dimensional Anderson model can not describe the impurity bath Green's function G_0 exactly, one finds the parameters ε_i and V_i by minimizing

$$\chi^2 = \frac{1}{n_{\max}} \sum_{n=0}^{n_{\max}} |G_0^{-1} - (G_0^{ED})^{-1}|^2.$$

When all parameters are determined we know the full Hamiltonian. To be able to calculate the interaction Green's function it is necessary to find the eigenvalues and eigenvectors of the Hamiltonian. We then write the creation and annihilation operators, and thereby the Hamiltonian, in terms of matrices. Because of the large size of the Hamiltonian we will use block-diagonalization to reduce the dimensions. Each block will be small enough in order to make the computer simulations reasonably fast. The block-diagonalization is done using symmetry properties. It is known that the particle number, the spin s_z, and the total spin s^2 of the system are conserved, which can be confirmed by computing $[H,\hat{N}] = 0$, $[H,\hat{S}_z] = 0$ and $[H,\hat{S^2}] = 0$. One can project the Hamiltonian into smaller blocks by using projectory matrices of the quantum numbers n, s_z and s^2. The eigenvalues of each block are the possible energies of a system with quantum numbers n_i, s_{zi} and s_i^2.

When all eigenstates and eigenvalues are determined the impurity Green's function $G_I(z)$ is given by

$$G_{I\sigma} = \frac{1}{Z}\sum_{\mu\nu}\frac{\langle\mu|c_\sigma^\dagger|\nu\rangle}{z+E_\mu-E_\nu}\left(E^{-\beta E_\nu}+E^{-\beta E_\mu}\right), \tag{6.6}$$

which is the Lehman spectral representation. The partition function in (6.6) can be evaluated as

$$Z = \mathrm{Tr}\left[E^{-\beta H}\right].$$

In this thesis only the case of zero temperature is considered. The terms that are non-zero in (6.6) contain the ground state, $\tilde{\mu}$, and are therefore given by

$$G_{I\sigma} = \frac{1}{n_{\mathrm{deg}}}\sum_{\tilde{\mu}\nu}\left(\frac{\langle\tilde{\mu}|c_\sigma^\dagger|\nu\rangle}{z+E_{\tilde{\mu}}-E_\nu}+\frac{\langle\nu|c_\sigma^\dagger|\tilde{\mu}\rangle}{z+E_\nu-E_{\tilde{\mu}}}\right), \tag{6.7}$$

where n_{deg} is the degeneracy of the ground state.

Equation (6.7) is used in exact diagonalization in order to compute the interaction Green's function given in (6.3). The formula was derived by applying Anderson mapping and the definition of Lehman spectral representation. From G_I the self-energy of impurity can be determined using the relation

$$\Sigma_I = G_0^{-1} - G_I^{-1}.$$

We have now covered the equations that are needed to solve an interacting many-body system when using ED. The next chapter will work as an overview of the DMFT algorithm.

6.3 Self-Consistent Equations

In this section the set of equations which DMFT consists of will be listed and then the self-consistent DMFT solution is discussed.

The algorithm of how to calculate the self-energy Σ_I of the impurity is given below.

1. Given an initial guess of the lattice self-energy $\Sigma_L(i\omega_n)$ and the known non-interacting density of states $\rho^{(0)}(\varepsilon)$, one can calculate the lattice Green's function G_L using the relation

$$G_L(i\omega_n) = \int d\varepsilon \frac{\rho^{(0)}(\varepsilon)}{i\omega_n - \varepsilon + \mu - \Sigma_L(i\omega_n)}.$$

2. The relation between local lattice Green's function and Σ_L in terms of the impurity bath Green's function is given by

$$G_0 = \left(G_L^{-1} + \Sigma_L\right)^{-1}.$$

3. The local impurity Green's function

$$G_{I\sigma\sigma'}(i\omega_n) = \int_0^\beta d\tau e^{i\omega_n\tau}\langle c_\sigma(\tau)c_{\sigma'}(0)\rangle_{S_{eff}[G_0]}.$$

   $G_{I\sigma\sigma'}$ is in our case obtained using the ED algorithm.

4. The sought self-energy of the impurity is now found by the relation

$$\Sigma_I(i\omega_N) = G_0^{-1}(i\omega_n) - G_I^{-1}(i\omega_n).$$

To summarize these steps we define a function $F : \Sigma_L \mapsto \Sigma_I$ (See Fig. 6.4). The fixed point solutions of the self-energies give the self-consistent DMFT solution,

$$F(\Sigma^*) = \Sigma^*.$$

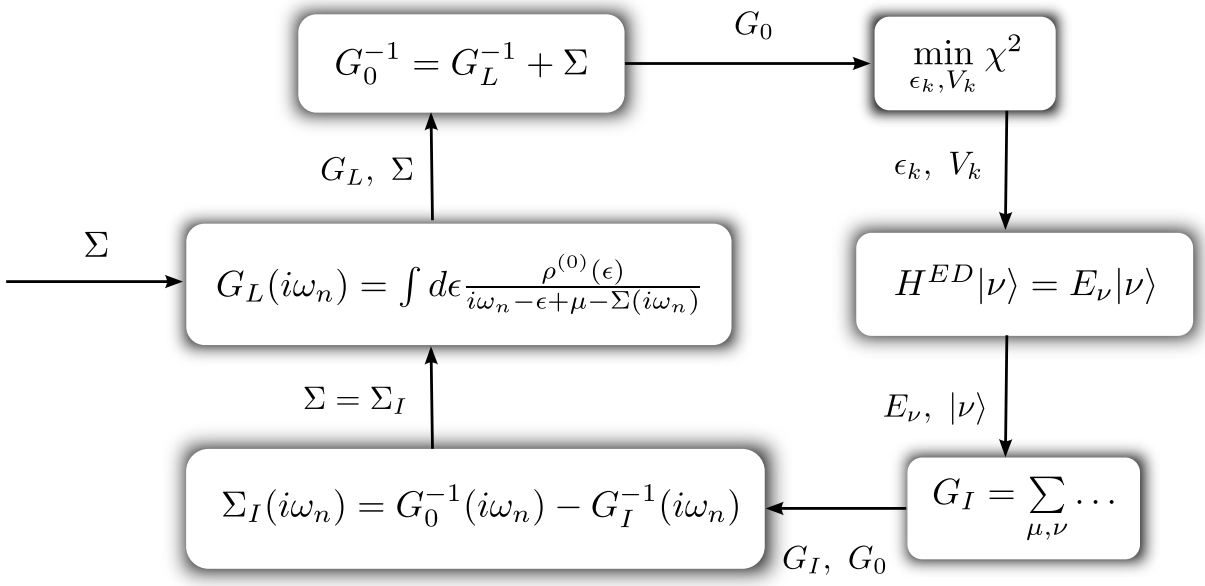

Figure 6.4. *A schematic representation of the self-consistent equations, when using ED as an impurity solver.*

7 Distributional Exact Diagonalization

The advantage of using distributional exact diagonalization (DistED) is that it enables calculation of the spectral function of a system without the need of an analytic continuation. This chapter explains the DistED scheme using what we already know about exact diagonalization.

DistED uses the ED algorithms, but instead of the fitting procedure used when minimizing the difference between the impurity bath Green's function and the Anderson Green's function, the local spectral function is used as a probability distribution for the sampling to find the parameters in the Anderson Hamiltonian. This is done in detail for the case of a Mott insulator which means an odd number of sites will be assumed. First we utilize the fact that for known coefficients $\{a_i,b_i\}$ there are unique solutions of the parameters $\{\varepsilon_i, V_i\}$ of the equation,

$$\left(z-\varepsilon_0+\mu-\sum_{i=1}^{n-1}\frac{V_i}{z-\varepsilon_i}\right)^{-1}=\sum_{j=1}^{n}\frac{a_j}{z-b_j}.$$

Thus the first step is to determine the coefficients $\{a_i,b_i\}$ of the Green's function on the form

$$G_0^\nu(z)=\sum_{i=1}^{n}\frac{a_i^\nu}{z-b_i^\nu}, \tag{7.1}$$

where $\{b_i\}_{i=1}^n$ are real values and the residue is normalized as $\sum_j a_j^\nu = 1$ for all ν. In other words, the coefficients $\{\varepsilon_i, V_i\}$ are found by determining the poles and residues of $G_0^\nu(z)$.

The first $(n-1)/2$ coefficients of $\{b_i\}_{i=1}^n$ in (7.1) are chosen randomly from a distribution represented by $\mathrm{Im}[G_0]/\pi = \mathrm{Im}[(G_L^{-1}+\Sigma)^{-1}]/\pi$. The other coefficients are then determined to satisfy the symmetry G_0^ν (one pole at $z=0$). The Green's function is then given by

$$G_0^\nu(z)=\sum_{i=1}^{(n-1)/2}\frac{a_i^\nu}{z-b_i^\nu}+\frac{a_{(n+1)/2}^\nu}{z}+\sum_{i=1}^{(n-1)/2}\frac{a_i^\nu}{z+b_i^\nu}. \tag{7.2}$$

To find relevant values of the residues one has to have in mind that the residue of the pole at $z=0$ is much larger than residues of other poles. So firstly, we explicitly set the residue $a_{(n+1)/2}^\nu$ to a nonrandom value according

to the weight at $z = 0$ in the spectral function:

$$a^{\nu}_{(n+1)/2} = \int_{-\delta}^{\delta} \frac{1}{\pi} \mathrm{Im}[G_0(\omega)] d\omega,$$

where δ in this case is a small number so that only the weight of the pole at $z = 0$ is included. The other residues are randomly chosen so that

$$a^{\nu}_{(n+1)/2} + \sum_{i=1}^{(n-1)/2} 2a^{\nu}_i = 1,$$

and this is because $\sum_{i=1}^{(n-1)/2} 2a^{\nu}_i \ll a^{\nu}_{(n+1)/2}$, i.e. these residues are not as significant as the residue of the pole at $z = 0$ when generating the Green's function.

Once the coefficients $\{a^{\nu}_i\}_{i=1}^{n}$ and $\{b^{\nu}_i\}_{i=1}^{n}$ are determined one can map $G^{\nu}_0(z)$ to the Green's function $G^{A,\nu}_0 = 1/(z - \varepsilon^{\nu}_0 + \mu - \sum_{i=1}^{n-1} \frac{V^{\nu}_i}{z-\varepsilon^{\nu}_i})$. The parameters ε^{ν}_i and V^{ν}_i are obtained by using

- $\varepsilon^{\nu}_0 = -\sum_j a^{\nu}_j b^{\nu}_j$,
- the solution to the equation $G^{\nu}_0(z = \varepsilon_i) = 0$,
- $V^{\nu}_i = \left(-\frac{\mathrm{d}G^{\nu}_0}{\mathrm{d}z}|_{\varepsilon^{\nu}_i}\right)^{-1/2}$.

When all parameters in the full Hamiltonian $H = H_0 - \mu \sum_\sigma c^\dagger_\sigma c_\sigma + U c^\dagger_\uparrow c^\dagger_\downarrow c_\uparrow c_\downarrow$ are determined, the same algorithm as in the ED method (explained in the previous chapter) is used to obtain $\Sigma^{\nu} - \mu = \left((G^{\nu}_0)^{-1} - (G^{\nu}_I)^{-1}\right)^{-1}$. The total self-energy can be approximated by the relation [3]

$$\Sigma_{tot} - \mu \approx \frac{1}{N} \sum_{\nu=1}^{N} (\Sigma^{\nu} - \mu) = \frac{1}{N} \sum_{\nu=1}^{N} \left((G^{\nu}_0)^{-1} - (G^{\nu}_I)^{-1}\right)^{-1}. \tag{7.3}$$

The evaluated self-energy is used to calculate a new G_L that will be the new input in the DMFT scheme, as illustrated in 6.4. When a converged self-energy Σ^* is found the sought self-energy of the real axis has been computed. Other than the self-energy it is also relevant to consider the density of states, which can be expressed as

$$A(\omega) = -\frac{1}{\pi}\mathrm{Im}[G_L] = -\frac{1}{\pi}\mathrm{Im}\left[\int d\epsilon \frac{\rho^{(0)}(\epsilon)}{i\omega_n - \epsilon + \mu - \Sigma_{tot}}\right].$$

Before applying DistED to a Mott insulator we will discuss the Mott metal-insulator transition (MIT).

7.1 Mott Metal-Insulator Transition

In the beginning of the 20th century the band theory was very successful in describing electrical properties of metals. It was found that there are some materials (with odd number of electrons per unit cell) which should, according to band theory, be conductors, but in reality proved to be insulators.

N. Mott and R. Peierls [5] predicted these materials to be insulators due to the strong Coulomb interactions between the electrons. This on-site Coulomb interaction causes a Mott metal-insulator transition (MIT).

A reason for the MIT to occur is that as the kinetic energy increases, the electron is more likely to move between different sites, which can lead to double occupied sites. However, if the interaction energy U is large, this behavior is largely prevented and may reduce the total energy of the system by localizing the electrons.

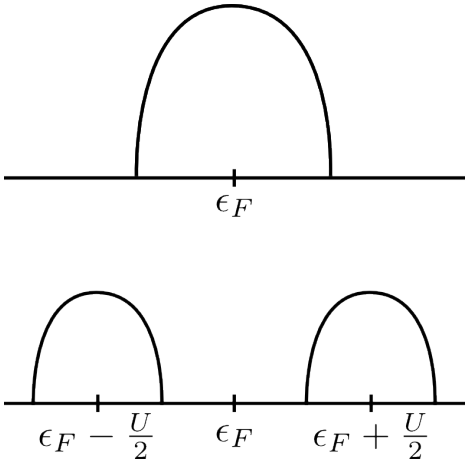

Figure 7.1. *An illustration of a metal-insulator transition.*

If we assume a small interaction energy U, then our spectral function $A(\omega)$ still resembles that of free electrons, which for the Mott insulator consists of two "Hubbard bands" at $\pm U/2$ (the bottom picture in Fig. 7.1). When decreasing U below a lower critical value the gap between the Hubbard bands vanishes (the top picture in Fig. 7.1). This describes a transition from an insulator to a metal.

At intermediate values of U the spectral function still has Hubbard bands but also a third peak at small energies, $\omega \approx 0$.

7.2 DistED Calculation of Mott Insulator

A half-filled Mott insulator will now be analysed using DistED with three sites ($n = 3$). The total self-energy and the density of states are calculated with the chemical potential $\mu = U/2$ and with the interaction energy $U = 4$

and $U = 10$. The number of samples ν has to be large for the self-consistency equations to converge. We set $\nu = 50\,000$ iterations.

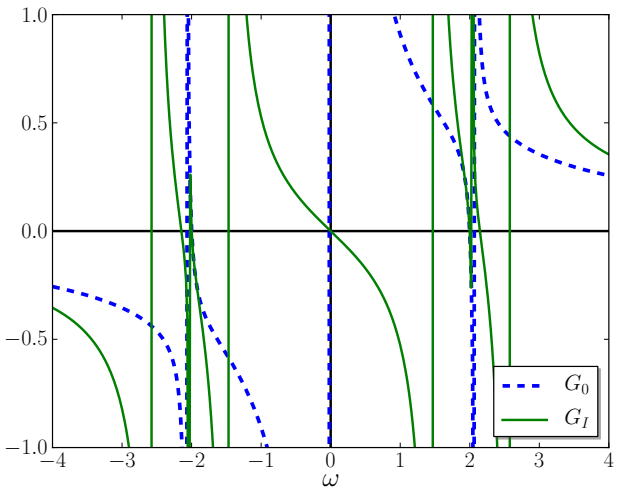

Figure 7.2. *The impurity Green's function together with the non-interaction Green's function when $U = 4$.*

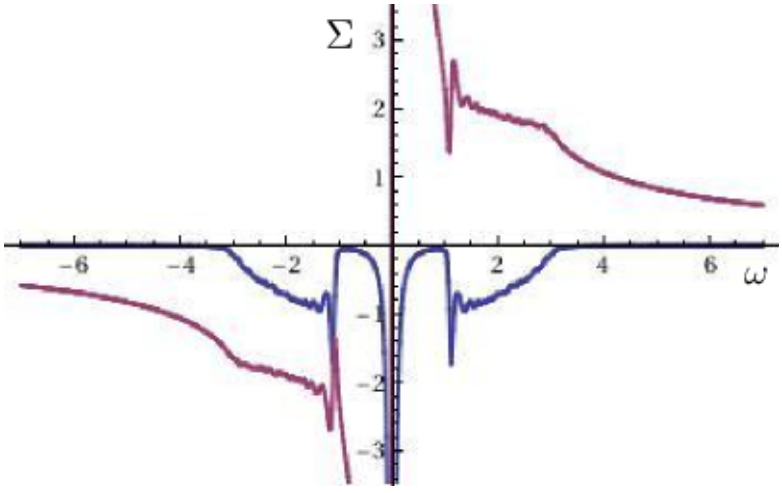

Figure 7.3. *The imaginary and real part of the self-energy for $U = 4$.*

To compute the impurity self-energy Σ we need the Green's functions G_I and G_0, which are plotted in Fig. 7.2. G_I has many more roots compared to the non-interacting Green's function G_0, and it is zero whenever G_0 is. We know that the impurity self-energy Σ has poles at points where G_I is zero and G_0 non-zero.

Firstly we investigate the Mott insulator when $U = 4$. Fig. 7.3 illus-

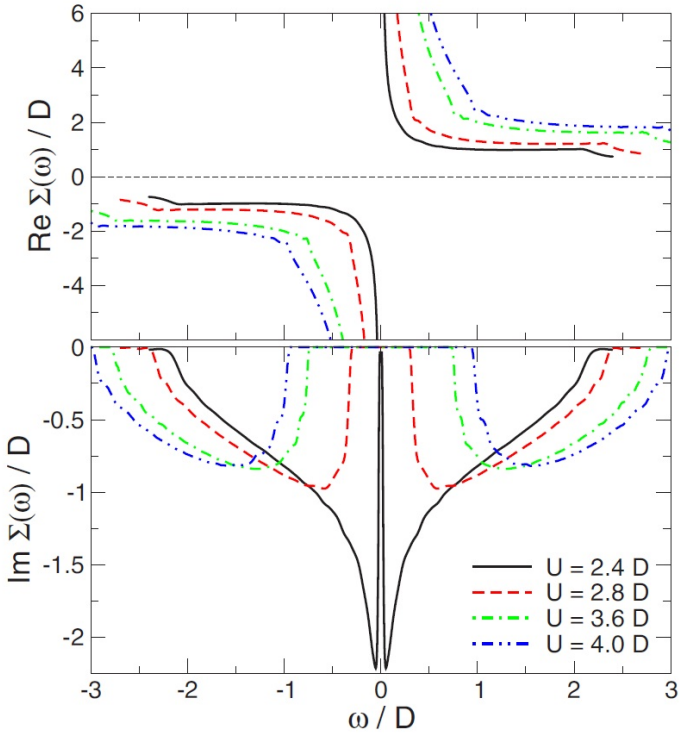

Figure 7.4. *The imaginary and real part of the self-energy using DRMG. Excerpted from M. Karski et al. [19], reproduced with permission.*

trates the real and imaginary part of the self-energy, Σ, when $U = 4$. The imaginary part of the self-energy is symmetric around $\omega = 0$ and is strictly less than zero. One also notices that the residue of the pole at $\omega = 0$ is large. These features are the consequence of having an insulating system with a symmetric G_0^{ν} and large weight at $\omega = 0$; similar results are shown for the same insulating system and with density-matrix renormalization group (DMRG) as an impurity solver [19] (See Fig. 7.4). What is interesting about Fig. 7.3 is the peaks at $\omega \approx \pm 1$, and as seen in Fig. 7.5 the same behavior appears for the density of states.

The density of states describes an insulator with two Hubbard bands located at $\pm U/2$, which is similar to the Hubbard bands in Fig. 7.1. However, in this case there are peaks in addition to the Hubbard bands. These results are intriguing since this kind of structure will not likely be found for some impurity solvers that require an analytic continuation, such as Maximum Entropy (MaxEnt), which assumes a smoother function of the self-energy. Some oscillations can also be seen in Fig. 7.5 due to noise.

In Fig. 7.6 the same system ($U = 4$ and $\beta = 20$)[1] is calculated with

[1]For detailed information about maxEnt and the parameter β see [20].

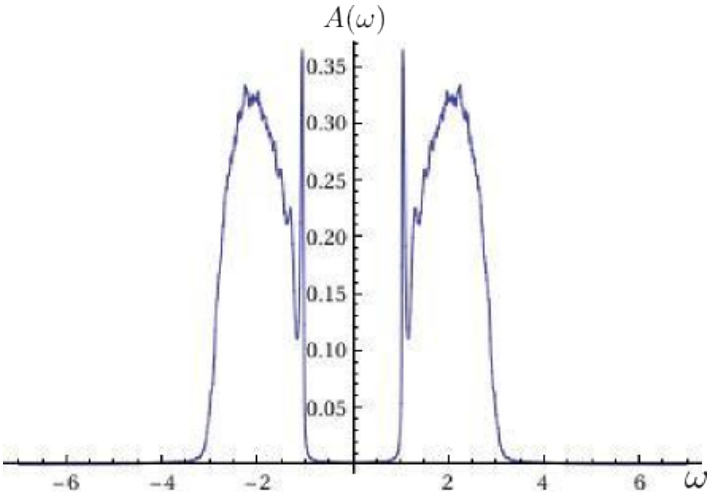

Figure 7.5. *The density of states for an insulator with $U = 4$.*

QMC as an impurity solver, and the MaxEnt method is used for the analytic continuation. This result shows a spectral function that is similar to Fig. 7.5; the width and height of the Hubbard bands are the same. The difference is that the peaks in Fig. 7.5 are not found by using the MaxEnt method.

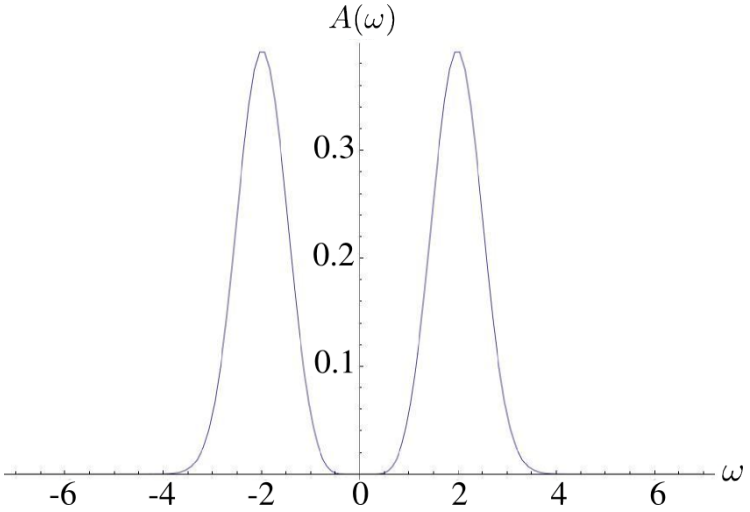

Figure 7.6. *The spectral function calculated with the maximum entropy method for $U = 4$ and $\beta = 20$. The graph is generated by Johan Schött, and reproduced here with permission.*

The second case that is treated in this thesis concerns an insulator with the interaction energy $U = 10$. Compared to $U = 4$, one notices that the weight of the imaginary part of the self-energy at $\omega = 0$ is larger for $U = 10$, as shown in Fig. 7.7. This is expected because having larger values

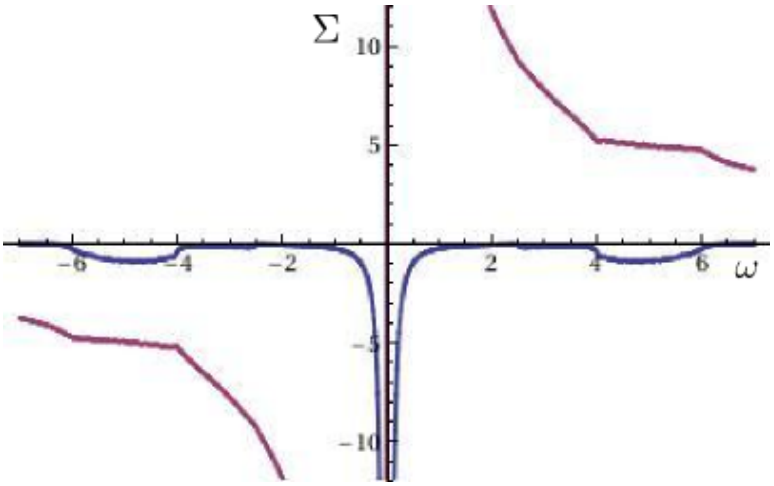

Figure 7.7. *The imaginary and real part of the self-energy for $U = 10$.*

of U leads to an increasing number of localized electrons. The density of states when the interaction energy $U = 10$ is plotted in Fig. 7.8. Here the Hubbard bands are located further away from each other compared to the case of $U = 4$. However, in both cases the Hubbard bands are located around $\omega = \pm U/2$. The results shown in Fig. 7.8 seem reasonable, due to the fact that the width of the Hubbard bands are approximately two and the integration over all frequencies is equal to one. The density of states for $U = 10$ does not have the peaks that were shown for $U = 4$. The exact result is known in the limit of large U, and does not have any peaks.

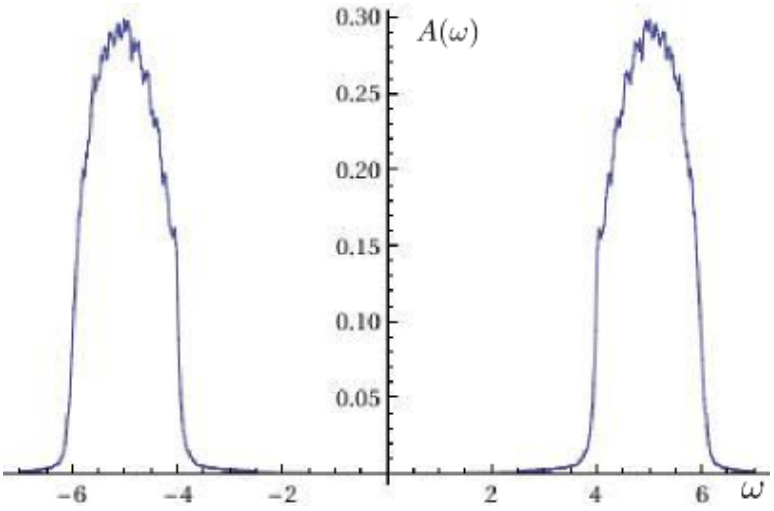

Figure 7.8. *The density of states for an insulator with $U = 10$.*

8 Conclusions

The distributional exact diagonalization formalism has been used to compute the analytic self-energy of a three-site Mott insulator. Initial studies using impurity solvers have shown that DistED gives good results for Mott insulators. The real part and imaginary part of the self-energy have similar behavior when calculated by either DistED or DMRG, and the density of states for interaction energy $U = 4$ has similar behavior as when using MaxEnt: the Hubbard bands are at $\omega = \pm U/2$. However, the peaks that appear in the density of states when using DistED do not appear when using MaxEnt (See Fig. 7.6).

We are not able to explain why the peaks occur, but it is interesting that this behavior is predicted by DistED whereas some methods using analytic continuation cannot detect them.

When $U = 10$, the Hubbard bands are located further apart from each other (at $\omega = \pm U/2$). It can also be noted that when the interaction energy is sufficiently large (as is the case when $U = 10$), the peaks that appeared for $U = 4$ are no longer present. In this case only two smooth Hubbard bands can be seen.

Bibliography

[1] A. Georges, G. Kotliar, W. Krauth and M. Rozenberg. *Dynamical mean-field theory of strongly correlated fermion systems and the limit of infinite dimension*, Rev. Mod. Phys. 68, 13–125 (1996).

[2] D. Vollhardt, K. Byczuk and M. Kollar, *Dynamical Mean-Field Theory*, in: Strongly Correlated Systems, ed. by A. Avella and F. Mancini, Springer Series in Solid-State Sciences, vol. 171, 203 (Springer, Berlin, Heidelberg, 2012).

[3] M. Granath and H.U.R Strand, *Distributional exact diagonalization formalism for quantum impurity models*, Phys. Rev. B 86, 115111 (2012).

[4] G. Kotliar and D. Vollhardt, *Strongly Correlated Materials: Insights From Dynamical Mean-Field Theory*, American Institute of Physics, March 2004.

[5] N.F. Mott and R. Peierls, *Discussion of the paper by de Boer and Verwey*, Proc. Phys. Soc. 49 72 (1937).

[6] J. Hubbard, *Electron Correlations in Narrow Energy Bands*, Proceedings of the Royal Society of London. Series A. Mathematical and Physical Sciences 276, 238 (1963).

[7] A. Sabashvili, *Periodized Thermal Greens Functions and Applications*. Licentiate thesis, University of Gothenburg, Sweden, 2013.

[8] C. Karasch, V. Meden and K. Schönhammer. *Finite-temperature linear conductance from the Matsubara Green's function without analytic continuation to the real axis*. Rev. Phys. B 82 (2010).

[9] John W. Negele and Henri Orland, *Quantum Many-Particle systems*, Westview Press, 1988.

[10] G.A. Baker, *Essentials of Padé Approximants*, Academic Press, New York, 27-38, 1975.

[11] D.A. Ryndyk, R. Gutiérrez, B. Song and G. Cuniberti, *Green Function Techniques in the Treatment of Quantum Transport at the Molecular Scale*, Springer Series in Chemical Physics Volume 93, 213-335 (2009).

[12] A.C. Hewson, *The Kondo Problem to Heavy Fermions*, Cambrigde University Press (1993).

[13] C. Karrasch, V. Meden and K. Schönhammer, *Finite-temperature linear conductance from the Matsubara Green's function without analytic continuation to the real axis*, Phys. Rev. B 82, 125114 (2010).

[14] W. Metzner and D. Vollhardt, *Correlated Lattice Fermions in $d = \infty$ Dimensions*, Phys. Rev. Lett. 62, 324 (1989).

[15] H.U.R. Strand, *Critical Properties of the Mott-Hubbard Metal-Insulator Transition*. Licentiate thesis, University of Gothenburg, Sweden, 2011.

[16] G. Kotliar, S.Y. Savrasov, K. Haule, V.S. Udovenko, O. Parcollet and C.A. Marianetti, *Electronic Structure Calculations with Dynamical Mean-Field Theory*, Rev. Mod. Phys. 78, 865-951 (2006).

[17] P. W. Anderson, *Localized Magnetic States in Metals*, Phys. Rev. 124, 41 (1961).

[18] M. Caffarel and W. Krauth, *Exact Diagonalization Approach to Correlated Fermions in Infinite Dimensions: Mott Transition and Superconductivity*, Phys. Rev. Lett. 72, 1545-1548 (1994).

[19] M. Karski, C. Raas and G.S. Uhrig, *Single-particle dynamics in the vicinity of the Mott-Hubbard metal-to-insulator transition*, Rev. Phys. B 77, (2008).

[20] M. Jarrell and J.E. Gubernatis, *Bayesian inference and the analytic continuation of imaginary-time quantum Monte Carlo data*, Physics Reports, 269, 133-195 (1996).